BIOCHEMISTRY
including biophysical chemistry & molecular biology

Article

pubs.acs.org/biochemistry

Conformational Preferences of DNA following Damage by Aristolochic Acids: Structural and Energetic Insights into the Different Mutagenic Potential of the ALI and ALII-N^6-dA Adducts

Preetleen Kathuria, Purshotam Sharma, Minette N. Abendong, and Stacey D. Wetmore*

Department of Chemistry and Biochemistry, University of Lethbridge, 4401 University Drive West, Lethbridge, Alberta, Canada T1K 3M4

Supporting Information

ABSTRACT: Aristolochic acids (AAI and AAII), produced by the Aristolochiaceae family of plants, are classified as group I (human) carcinogens by the International Agency for Research on Cancer. These acids are metabolized in cells to yield aristolactams (ALI and ALII, respectively), which further form bulky adducts with the purine nucleobases. Specifically, the adenine lesions are more persistent in cells and have been associated with chronic renal diseases and related carcinogenesis. To understand the structural basis of the nephrotoxicity induced by AAs, the ALI-N^6-dA and ALII-N^6-dA lesions are systematically studied using computational methods. Density functional theory calculations indicate that the aristolactam moiety intrinsically prefers a planar conformation with respect to adenine. Nucleoside and nucleotide models suggest that the *anti* and *syn* orientations about the glycosidic bond are isoenergetic for both adducts. Molecular dynamics simulations and free energy calculations reveal that the *anti* base-displaced intercalated conformation is the most stable conformer for both types of AL-N^6-dA adducted DNA, which agrees with previous experimental work on the ALII-N^6-dA adduct and thereby validates our approach. Interestingly, this conformer differs from the dominant conformations adopted by other N6-linked adenine lesions, including those derived from polycyclic aromatic hydrocarbons. Furthermore, the second most stable *syn* base-displaced intercalated conformation lies closer in energy to the *anti* base-displaced intercalated conformation for ALI-N^6-dA compared to ALII-N^6-dA. This indicates that a mixture of conformations may be detectable for ALI-N^6-dA in DNA. If this enhanced conformational flexibility of double-stranded DNA persists when bound to a lesion-bypass polymerase, this provides a possible structural explanation for the previously observed greater nephrotoxic potential for the ALI versus ALII-N^6-dA adduct. In addition, the structural characteristics of the preferred conformations of adducted DNA explain the resistance of these adducts to repair and thereby add to our current understanding of the toxicity of AAs within living cells.

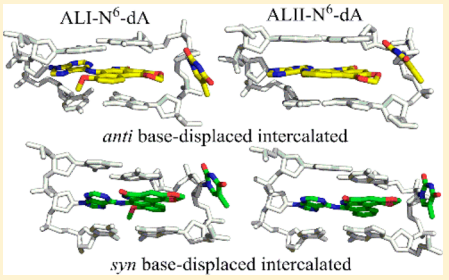

Aristolochic acids, chemically nitrophenanthrene carboxylic acids, are potent carcinogens and established nephrotoxins that originate from the Aristolochiaceae family of plants. The major components of extracts from these plants are aristolochic acids I and II (AAI and AAII, respectively), which differ in the presence or absence of a methoxy group (Figure 1a). These toxins have been determined to be responsible for Chinese herb nephropathy (CHN), a rapidly progressive kidney fibrosis associated with the prolonged intake of Chinese herbs contaminated with *Aristolochia fangchi*.[1] In addition, exposure to AAs has been linked to Balkan endemic nephropathy (BEN) through the consumption of locally grown wheat contaminated with seeds from *Aristolochia clematitis*.[2,3] Because of the striking similarities in the clinical expression and pathology of lesions associated with CHN and BEN, the term aristolochic acid nephropathy (AAN) is now proposed to cover both conditions.[4] In addition to their nephrotoxic potential, exposure to AAs has been associated with urothelial carcinoma in the upper urinary tract (UUC).[5−7] Because of their potential carcinogenic effects, the International Agency for Research on Cancer (IARC) categorized herbal medicines containing the plant species of the *Aristolochia* genus as Group 1 (human) carcinogens.[8]

Pioneering experimental work independently initiated by Grollman, Schmeiser, and collaborators,[6,9−17] has shed light on important aspects of the bioactivation of AAs and their relation to BEN. In particular, the metabolic activation of AAs has been shown to involve the NAD(P)H:quinone oxidoreductase-catalyzed reduction of the nitro group to yield *N*-hydroxyaristolactams (*N*-hydroxy ALs), which further hydrolyze to form nitrenium ions.[13,15,16] These intermediates specifically attack the purine DNA nucleobases to form the AL-N^6-dA (Figure 1a) and AL-N^2-dG adducts,[15,17] which were identified in the renal tissues of patients affected by BEN.[10] Furthermore, the AA-initiated carcinogenesis is associated with "signature" A → T mutations,[11,18,19] which are dominant in the TP53 tumor suppressor gene[10] and the FGFR3 or HRAS oncogene.[6] *In vitro* studies of the replication and repair of these adducts indicate

Received: December 3, 2014
Revised: February 4, 2015
Published: March 11, 2015

DOI: 10.1021/bi501484m
Biochemistry 2015, 54, 2414−2428

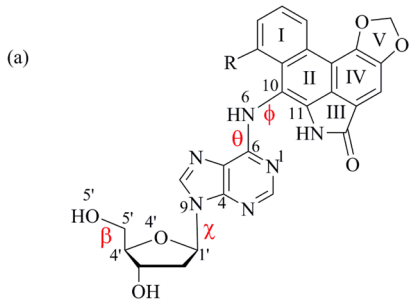

Figure 1. (a) Structure of the AL-N^6-dA adducts (R = OCH_3 for ALI and H for ALII). The θ [$\angle$(N1C6N6C10)] and ϕ [$\angle$(C6N6C10C11)] dihedral angles determine the orientation of the AL moiety with respect to base; χ [$\angle$(O4′C1′N9C4)] dictates the glycosidic bond orientation to be *syn* ($\chi = 0 \pm 90°$) or *anti* ($\chi = 180 \pm 90°$), and β [$\angle$(C4′C5′O5′H5′)] governs the sugar−phosphate backbone orientation. (b) The 11-mer DNA sequence used for MD simulations with the adduct at the X^6 position.

that while both lesions misincorporate A, only AL-N^6-dA persists in cells,[9] possibly because of its greater resistance to repair by the global genomic repair pathway compared to that of AL-N^2-dG.[14]

Despite the known mutagenicity of the AL-N^6-dA lesions and abundance of literature on the structurally similar N^6-linked PAH adenine lesions,[20−30] to the best of our knowledge, only one recent study has analyzed the structural characteristics of damaged DNA containing the ALII-N^6-dA adduct using NMR spectroscopy.[31] Surprisingly, unlike most N^6-dA linked PAH lesions, which intercalate the bulky moiety into DNA without displacing the opposing base,[20,23,24] intercalation of the ALII moiety displaces the opposing thymine into the major groove. This raises an important question regarding the structural and energetic features that drive the differential conformational outcomes of the ALII-N^6-dA lesion compared to those of the PAH adducts. Furthermore, despite the higher abundance[16,32,33] and greater nephrotoxic potential[34] of AAI compared to those of AAII in cells, recent studies have focused on the properties of the ALII-N^6-dA lesion.[9,14,31] However, previous studies of other DNA adducts (e.g., on C8-AF-dG,[35−37] C8-AAF-dG,[35,37−40] and PAH[20−23] adducts) have shown that subtle changes in the chemical structure of the lesion may have profound implications for its conformation and mutagenicity within DNA. Therefore, the effect of the methoxy group present in ALI-N^6-dA on the conformational outcomes of adducted DNA must be investigated.

This work undertakes a systematic molecular modeling study, including quantum chemical [density functional theory (DFT)] methods, molecular dynamics (MD) simulations, and free energy analysis, to explore and compare the conformational space of the ALI-N^6-dA and ALII-N^6-dA lesions. Specifically, the nucleobase, nucleoside, and nucleotide adducts are considered to determine the preferred orientation of the bulky moiety with respect to the base and the *anti*/*syn* preference. Subsequently, the adducts are incorporated into an 11-mer oligonucleotide opposite complementary thymine, and MD simulations are conducted to reveal the effects of the helical environment on the *anti*/*syn* conformational preference. Our approach is validated through careful comparison to NMR structural data previously published for the ALII-N^6-dA lesion.[31] As a result, our work reliably predicts for the first time the effect of the additional methoxy group present in the ALI-N^6-dA lesion on the conformational preferences of AA adducted DNA. Furthermore, the preferred conformations of adducted DNA are analyzed in detail, which provides a structural basis for the resistance of the AL-N^6-dA lesions to be repaired by NER machinery. Overall, our work yields valuable structural insights into the experimentally observed differences in the mutagenic potentials and persistence of the AL-N^6-dA adducts.

MATERIALS AND METHODS

Nucleobase Model. To build the nucleobase model, the AL moiety formed from AAI or AAII was attached to the N6 position of adenine. Although both AL-N^6-A adducts can exist in the amino or imino tautomeric form at the N6 position,[41] a recent combined experimental and modeling study concluded that the amino form predominates in DNA.[31] For this reason, only the amino form is considered in this work. The relative orientation of the AL moiety with respect to the nucleobase is dictated by rotation about two dihedral angles, θ [$\angle$(N1C6N6C10)] and ϕ [$\angle$(C6N6C10C11)] (Figure 1a). Therefore, the B3LYP/6-31G(d) potential energy surface (PES) was initially mapped as a function of θ and ϕ. Full optimizations were subsequently performed on all minima identified from the PES using B3LYP/6-31G(d) and the dispersion-corrected B3LYP-D3/6-31G(d). Finally, B3LYP and B3LYP-D3 were used in conjunction with the 6-311+G(2df,p) basis set to obtain more accurate relative energies.

Nucleoside Model. The nucleoside model was built by adding 2′-deoxyribose in the B-DNA relevant C2′-endo puckering to the lowest-energy conformation obtained from the nucleobase model. Addition of the sugar moiety increases the complexity of the model because dihedral angle χ [$\angle$(O4′C1′N9C4)] (Figure 1a) must also be considered, which determines the orientation of the base about the glycosidic bond. Nevertheless, the nucleobase model indicates that the energy does not change significantly upon rotation about ϕ. Therefore, the gas-phase B3LYP/6-31G(d) PES of the nucleoside adduct was scanned with respect to θ and χ. The ε = $\angle$(C4′C3′O3′H5′) torsion angle (Figure 1a) was initially set to approximately 180°, which is the average value obtained from previous MD simulations on the Dickerson−Drew dodecamer.[42] The minima obtained from the PES were fully optimized using B3LYP and B3LYP-D3 with the 6-31G(d) basis set, and the same functionals were used with 6-311+G(2df,p) to obtain more accurate relative energies. Furthermore, B3LYP-D3/6-31G(d) optimizations, followed by B3LYP-D3/6-311+G(2df,p) single-point calculations, were performed on the lowest-energy *anti* and *syn* conformations while the β dihedral angle was geometrically constrained to 180°, which permits analysis of DNA relevant conformations of the adduct.

Nucleotide Model. To generate the initial nucleotide model, a 5′-monophosphate group was added to the lowest-energy *anti* and *syn* conformers identified from the nucleoside model. A previous study indicates that the DNA relevant geometries of the nucleotide model are obtained only when the solvent (water) environment and a Na^+ counterion are used during the optimization routine.[43] Therefore, the nucleotide model was optimized in water (ε = 78.4) using IEF-PCM-B3LYP/6-31G(d) and the UFF radii to build the molecular

DOI: 10.1021/bi501484m
Biochemistry 2015, 54, 2414−2428

cavity for solvation. Single-point calculations were performed with IEF-PCM-B3LYP-D3/6-311+G(2df,p).

Because of good agreement between the results obtained from B3LYP and B3LYP-D3, the B3LYP-D3 data are presented in the main text for the nucleobase and nucleoside models, while B3LYP results can be found in the Supporting Information (Tables S1−S3). Coordinates of all nucleobase minima and the lowest-energy *anti* and *syn* minima for the nucleoside, *β*-constrained nucleoside, and nucleotide models are provided in the Supporting Information (Tables S4−S27). All reported DFT (B3LYP and B3LYP-D3) relative energies include a scaled (0.9806) zero-point vibrational energy correction. All quantum mechanical calculations were performed using Gaussian 09 (revision C.01 or D.01).[44,45]

DNA Model. *DNA Sequence.* The 11-mer oligonucleotide 5′-CGTACXCATGC [X = adduct (Figure 1b)] was used in the MD simulations. This sequence was chosen on the basis of previous experimental studies that suggest ALII-N^6-dA adducted DNA is most stable when cytosine flanks the lesion.[31] In addition, this sequence was used in a previous NMR study of ALII-N^6-dA adducted DNA,[31] which allows direct comparison to our simulations. Moreover, other structurally similar N6-linked adenine PAH adducts have also been studied in a similar sequence context,[20,24,25] which allows us to determine the effect of the chemical composition of the bulky moiety on the conformational preferences. In addition to the (CXC) sequence context studied here, two other (T/CXG) mutational hot spots are known in the context of aristolochic acids.[11,18] However, the main aim of this study is to carefully characterize all possible conformations that are accessible to ALI-N^6-dA- and ALII-N^6-dA adducted DNA and to compare relative flexibilities of the two damaged strands. To best achieve this goal, we focus on only one sequence in this work, which is the experimentally determined most stable sequence for ALII-N^6-dA adducted DNA.[31]

Starting Structures. The initial model for Arnott B-form DNA was built using the NAB[46] module of the AMBER package.[47,48] Adenine initially present at the X position in the natural DNA sequence was modified at N6 using GaussView[49] by attaching the ALI or ALII moiety formed from AAI or AAII, respectively. Initial conformations of the adducts within DNA were built on the basis of the lowest-energy *anti*/*syn* structures obtained from the nucleotide model, while avoiding steric clashes with the surrounding nucleotides, and the damaged base was paired against complementary T. To adequately sample the conformational space of the adducted DNA, trial simulations were conducted with various starting structures, which differ in the location of the bulky moiety in the helical environment. Final production simulations were subsequently initiated from representative conformations obtained from these trial simulations.

Force Field. The adducted DNA was neutralized with 20 sodium ions and then solvated in an 8 Å octahedral box of TIP3P water, which corresponds to near physiological conditions (Table S28 of the Supporting Information).[50] Although force fields that afford improved descriptions of monovalent ions are available,[51−53] a previous study indicates that simulations at low ion concentrations or at near physiological conditions are robust regardless of the ion model implemented.[54] For this reason, we used the parm94 parameters for sodium ions in this work, which are the default choice in AMBER 11 or 12. Partial atomic charges for ALI-N^6-dA and ALII-N^6-dA were calculated with RED.v.III.4,[55] using the HF/6-31G* and the RESP-A1 scheme. ANTECHAMBER 1.4[56] was used to assign atom types (Tables S29 and S30 of the Supporting Information). The parambsc0[57] modification of the parm99[58] force field was used to simulate the natural and adducted nucleotides, while additional parameters for the N6 moiety of the adducted nucleotides were taken from the General Amber Force Field (GAFF).[59] Although the χ_{OL} parameter set has recently been developed to improve the description of *syn* nucleotides in RNA (i.e., in loops or unpaired regions),[60] the use of χ_{OL} worsens the description of B-DNA (i.e., distorts the helical parameters and sugar pucker compared to those of X-ray crystal structures).[60,61] Because this conformational study focuses on damaged B-DNA helices, the χ_{OL} parameters were not used to avoid such distortions. Furthermore, we are confident that the parm99 parameters provide an adequate description of the AL-N^6-dA adducts in DNA because (1) the bulky moiety is positioned away from the glycosidic bond, which ensures that the χ profile of adenine does not change upon adduct formation (see Figure S1 of the Supporting Information), and (2) the stacking of the bulky moiety in DNA locks the χ value of the adduct in MD simulations close to the value obtained from the DFT models (Table S31 of the Supporting Information).

Simulation Details. Each DNA system was initially minimized using 500 steps of steepest descent followed by 500 steps of conjugate gradient minimization, with a 500 kcal mol^{-1} Å^{-2} restraint on DNA. Subsequently, minimization was performed using 1000 steps of steepest descent followed by 1500 steps of conjugate gradient minimization with no restraints. The system was then heated to 300 K with the DNA restrained using a force constant of 10 kcal mol^{-1} Å^{-2}, and a 20 ps constant-volume MD simulation was performed. Production simulations were subsequently run for 20 ns starting from DNA conformations obtained from trial simulations using the PMEMD[62] module of AMBER 11[48] or AMBER 12.[47] All final production simulations gave rise to stable structures with a maximal standard deviation of 0.9 Å in the backbone rmsd (see Figure S2 of the Supporting Information).

To analyze the structural features at the lesion site for each distinct conformation of adducted DNA, the step parameters were calculated using a pseudostep consisting of the base pairs 5′ and 3′ with respect to the lesion. A pseudostep was used for analysis because the disrupted AL-N^6-dA:T pair cannot be used to calculate the step parameters at the lesion site due to intercalation of the AL moiety. The pseudostep parameters thus calculated markedly differ from the step parameters defined for natural DNA according to adjacent base pairs. For example, the twist angle calculated using a pseudostep is almost double (∼60°) (Table S32 of the Supporting Information) the average twist in natural DNA (∼30°)[63] calculated using adjacent base pairs.

To confirm convergence of key structural parameters at the lesion site, we extended the production simulations of the *syn*/*anti* base-displaced intercalated conformations, as well as the natural (control) helix, by 300 ns. The structures do not deviate significantly between the 20 and 320 ns simulations (Table S32 of the Supporting Information), which provides confidence in the reported results. Most importantly, the distribution in the pseudotwist angle, which affects the stacking energies at the lesion site and therefore the relative stabilities of the adducted DNA conformations, agrees very well between the 20 and 320 ns simulations (see Figure S3 of the Supporting Information).

DOI: 10.1021/bi501484m
Biochemistry 2015, 54, 2414−2428

A unimodal distribution was obtained with respect to the χ, θ, and ϕ dihedral angles of the adduct throughout each simulation (Figures S4−S7 of the Supporting Information). Therefore, a single representative structure was obtained from each simulation by clustering the entire trajectory with respect to the position of the atoms forming θ, χ, and ϕ using the PTRAJ module of AMBER 11.[48] Pseudostep parameters and van der Waals interaction energies at the lesion site were calculated using the "nastruct" and "lie" commands of CPPTRAJ module of AMBER 12, respectively. Free energies were calculated from each simulation trajectory using the MM-PBSA[64] method, which compares well with the more rigorous umbrella sampling method.[65] In these calculations, snapshots were taken at 50 ps intervals over the entire simulation (400 frames in total), and the entropy term was estimated using the normal-mode analysis method.

RESULTS

Flexibility of the Nucleobase Adduct. The ALI and ALII nucleobase adducts were investigated to determine the preferred orientation of the bulky moiety with respect to the base. The PES with respect to θ and ϕ for both ALI-N^6-A and ALII-N^6-A (Figure 2a,b) indicate that for a given ϕ, a planar orientation about the C6−N6 bond ($\theta \sim 0°$ or 180°) is more stable than the orthogonal orientation ($\theta \sim 90°$ or 270°). The two minima at $\theta \sim 0°$ ($\phi \sim 30°$ or 330°) are separated by a low (<10 kJ mol^{-1}) rotational barrier with respect to ϕ (Figure 2a,b). On the other hand, the two minima at $\theta \sim 180°$ ($\phi \sim 60°$ or 300°) are separated by a higher rotational barrier (~20 kJ mol^{-1}). The interconversion between a minimum at $\theta \sim 0°$ and a minimum of $\theta \sim 180°$ is associated with a large energetic penalty (~40−60 kJ mol^{-1}), with ALII-N^6-A exhibiting greater flexibility about θ than ALI-N^6-A. Thus, the ϕ dihedral angle is inherently more flexible than θ.

Upon full optimization (Figure 2c,d), the global minimum for ALI-N^6-A (ALII-N^6-A) occurs at θ = 12.4° (5.2°) and ϕ = 327.0° (322.4°). In addition, a nearly isoenergetic minimum is obtained through rotation about ϕ by ~70°. On the other hand, two isoenergetic minima ($\theta \sim 180°$ and $\phi \sim 50−60°$ or 295−305°) are ~8−13 kJ mol^{-1} less stable than the global minimum. The larger energetic difference in the case of ALI-N^6-A is due to the loss of two hydrogen bonds in ALI-N^6-A versus a single hydrogen bond in ALII-N^6-A upon rotation about θ. Nevertheless, the energy difference is smaller than the strength of the hydrogen bond(s) because the loss of the stabilizing interactions in the higher-energy minima ($\theta \sim 180°$) is partially compensated by reduced steric repulsion at $\theta \sim 180°$ compared to the global minimum ($\theta \sim 0°$). Overall, the small energetic differences between minima indicate that the AL-N^6-A adducts possess significant conformational flexibility at the nucleobase level.

Flexibility of the Nucleoside Adduct. The ALI-N^6-dA and ALII-N^6-dA nucleoside adducts were built by adding a deoxyribose to the corresponding nucleobase global minimum to determine the conformational flexibility at the glycosidic bond and the *anti*/*syn* energetic preference. Seven minima can be located on the PES of the ALI-N^6-dA and ALII-N^6-dA adducts when considered as a function of the χ and θ dihedral angles (Figures 3a and 4a). For both adducts, the global minimum adopts the *syn* orientation, while the corresponding *anti* conformers are approximately 20−30 kJ mol^{-1} higher in energy. Nevertheless, interconversion between the lowest-energy *anti* and *syn* minima (rotation with respect to χ) is

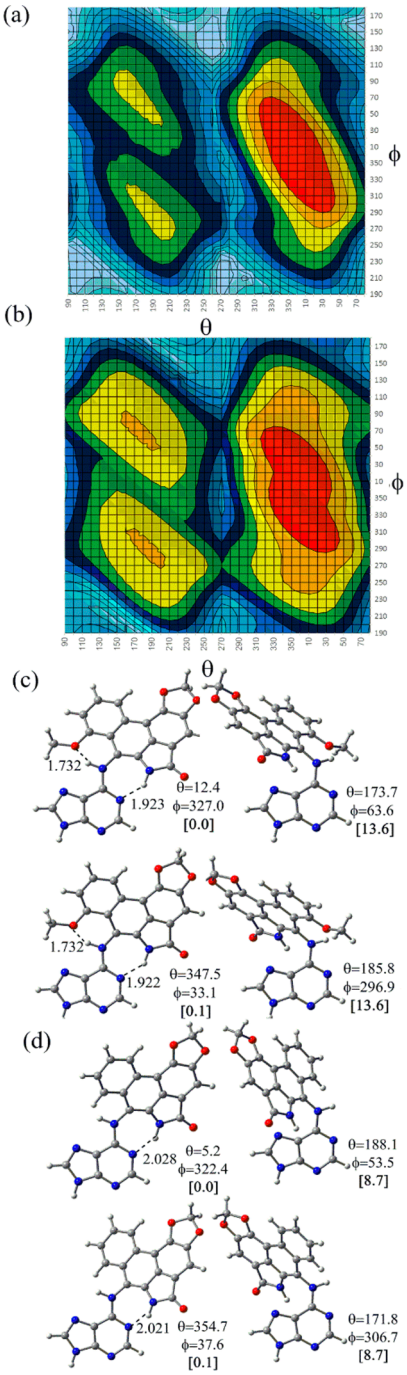

Figure 2. B3LYP/6-31G(d) potential energy surfaces (PES) for the (a) ALI-N^6-A and (b) ALII-N^6-A nucleobase adducts. B3LYP-D3/6-31G(d) optimized minima, bond lengths (Å), dihedral angles (degrees), and the corresponding B3LYP-D3/6-311+G(2df,p) relative energies (in brackets, kJ mol^{-1}) for the (c) ALI-N^6-A and (d) ALII-N^6-A nucleobase adducts are provided.

energetically more favorable than that between two *syn* minima (rotation with respect to θ). This is due to regions of high steric repulsion encountered at $\theta \sim 270°$ and 90°. Thus, the AL-N^6-dA nucleoside adducts are more flexible with respect to χ than θ.

The nucleobase model indicates that two nearly isoenergetic ϕ values are possible for a given θ. Therefore, for each of the seven minima on the χ versus θ PES, a second conformer is possible that differs in ϕ, such that ϕ = 30−60° or 330−300°.

DOI: 10.1021/bi501484m
Biochemistry 2015, 54, 2414−2428

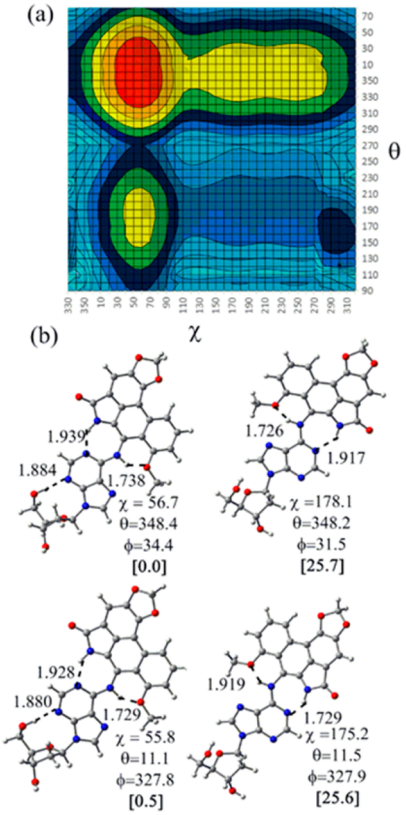

Figure 3. (a) B3LYP/6-31G(d) potential energy surface (PES) and (b) B3LYP-D3/6-31G(d) fully optimized lowest-energy *anti* and *syn* minima with the two possible ϕ values for the ALI-N^6-dA adduct. Select bond lengths (Å), dihedral angles (degrees), and the corresponding B3LYP-D3/6-311+G(2df,p) relative energies (in brackets, kJ mol^{-1}) are provided.

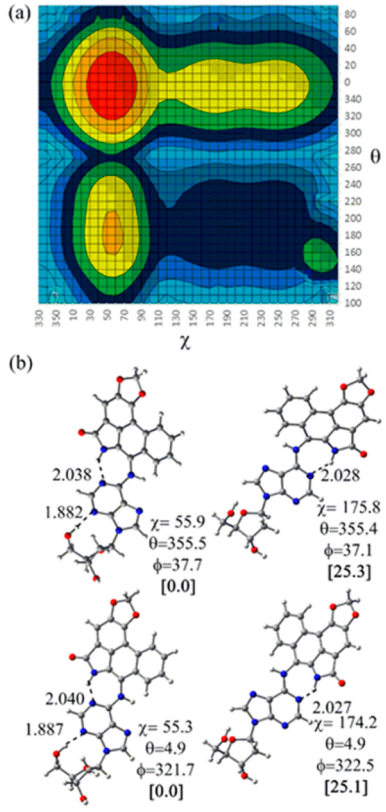

Figure 4. (a) B3LYP/6-31G(d) potential energy surface (PES) and (b) B3LYP-D3/6-31G(d) fully optimized lowest-energy *anti* and *syn* minima with the two possible ϕ values for the ALII-N^6-dA adduct. Select bond lengths (Å), dihedral angles (degrees), and the corresponding B3LYP-D3/6-311+G(2df,p) relative energies (in brackets, kJ mol^{-1}) are provided.

Thus, a total of 14 fully optimized minima were characterized for each adduct (Figures S8−S11 of the Supporting Information), where the lowest-energy *anti* and *syn* minima for each possible ϕ value are shown in Figures 3b and 4b. Regardless of the ϕ value considered, the fully optimized global (*syn*) minimum for both adducts ($\chi \sim 55°$, and $\theta \sim 350°$) is ∼8−14 kJ mol^{-1} lower in energy that the *syn* minimum related by rotation about θ ($\chi \sim 55°$, and $\theta \sim 180°$), primarily because of differences in intramolecular hydrogen bonding. On the other hand, the lowest-energy *anti* minimum ($\chi \sim 180°$, and $\theta \sim 350°$) is ∼25 kJ mol^{-1} less stable than the global *syn* minimum. This *anti* minimum is nearly isoenergetic to a second *anti* minimum that primarily differs in χ (∼255°), which reflects the fact that change in χ does not affect interactions between adenine and the AL moiety. The three remaining *anti* minima are (∼40 kJ mol^{-1}) less stable than the global *syn* minimum because of the lack of hydrogen bonds among the sugar, nucleobase, and/or the AL moiety. Because the structures with $\phi = 30-60°$ are lower (if not equal) in energy to those with $\phi = 330-300°$ for a given combination of χ and θ, subsequent models consider only initial structures with ϕ ranging between 30° and 60°.

Closer examination of the lowest-energy *syn* and *anti* conformations reveals that the global *syn* conformer possesses an additional hydrogen bond between the 5′-OH of the sugar and N3 of the nucleobase that is absent in the *anti* conformation (Figures 3b and 4b). Although this interaction may affect the *anti*/*syn* relative stability, it is relevant only when the adduct is located at the 5′-terminal end of DNA because the 5′-OH is replaced by a 5′-phosphate group at all other helical positions. To analyze the conformation of the adduct at other helical positions, the lowest-energy *anti* and *syn* conformations (with $\phi = 30-60°$) were reoptimized while the β dihedral angle (Figure 1a) was geometrically constrained to 180°. The most significant structural changes upon optimization occur in the *syn* form because of the repulsions between O5′ of the sugar and the nucleobase moiety. More importantly, removal of the O5′−H···N3 interaction increases the energy of the *syn* conformer such that the *anti* orientation is ∼11 kJ mol^{-1} more stable (Figure 5). Nevertheless, this small *anti*/*syn* energy difference indicates that the adducted nucleosides may possess flexibility at the glycosidic bond within DNA.

Flexibility of the Nucleotide Adduct. Because the small difference in the *anti*/*syn* stability for the nucleoside model may be altered by the 5′-phosphate group in DNA, a phosphate group was added to the lowest-energy *anti* and *syn* β-constrained nucleoside conformations (Figure 6). In the previously studied nucleotide models of the C8-OTB-dG[66] and C8-phenoxyl-dG[43] adducts, the phosphate moiety interacts with either the bulky group or the nucleobase, which alters the *anti*/*syn* energy difference. In contrast, our calculations indicate that such base−phosphate or phosphate−bulky moiety interactions are absent in the AL-N^6-dA adducts. Therefore, the incorporation of a phosphate group decreases the *anti*/*syn* energy difference such that the *anti* conformation is marginally more stable (by ∼6 kJ mol^{-1}). Nevertheless, there is no

DOI: 10.1021/bi501484m
Biochemistry 2015, 54, 2414−2428

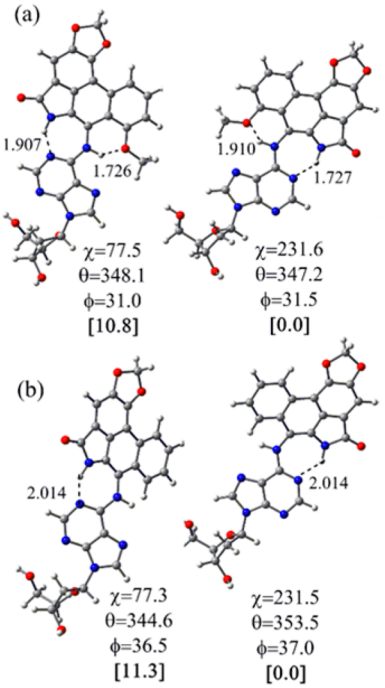

Figure 5. B3LYP-D3/6-31G(d) lowest-energy *anti* and *syn* minima for the (a) ALI-N^6-dA and (b) ALII-N^6-dA β-constrained nucleoside adducts. Select bond lengths (Å), dihedral angles (degrees), and the corresponding B3LYP-D3/6-311+G(2df,p) relative energies (in brackets, kJ mol^{-1}) are provided.

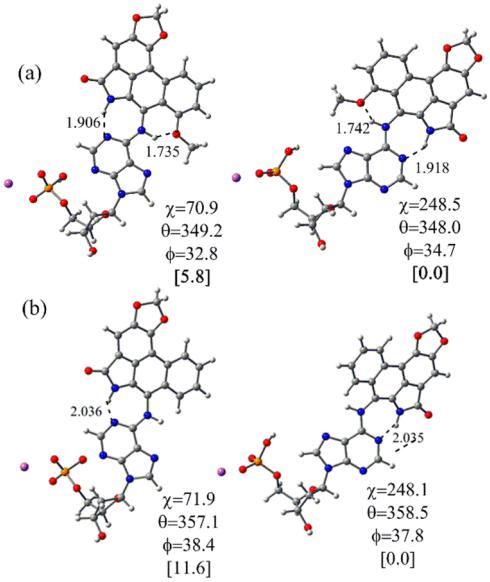

Figure 6. PCM-B3LYP-D3/6-31G(d) lowest-energy *anti* and *syn* minima for the (a) ALI-N^6-dA and (b) ALII-N^6-dA nucleotide adducts. Select bond lengths (Å), dihedral angles (degrees), and the corresponding B3LYP-D3/6-311+G(2df,p) relative energies (in brackets, kJ mol^{-1}) are provided.

significant effect on key structural features for the AL-N^6-dA nucleotide models compared to the DNA relevant β-constrained nucleoside model. This small *anti*/*syn* energy difference may be further affected by the presence of flanking nucleotides, and therefore, both the *anti* and *syn* conformations must be considered in DNA.

Flexibility of Adducted DNA. *Structural Features of Possible Conformations of Adducted DNA.* MD simulations of the ALI and ALII-N^6-dA adducts (X) in the 5′-CGTACX-CATGC 11-mer paired against T (Figure 1b) were initiated from various input structures to sample the conformational space. As a result, three distinct conformations for each of the *anti* and *syn* adducted nucleotide orientations were characterized for both adducts (Figures 7 and 8). The first structure is

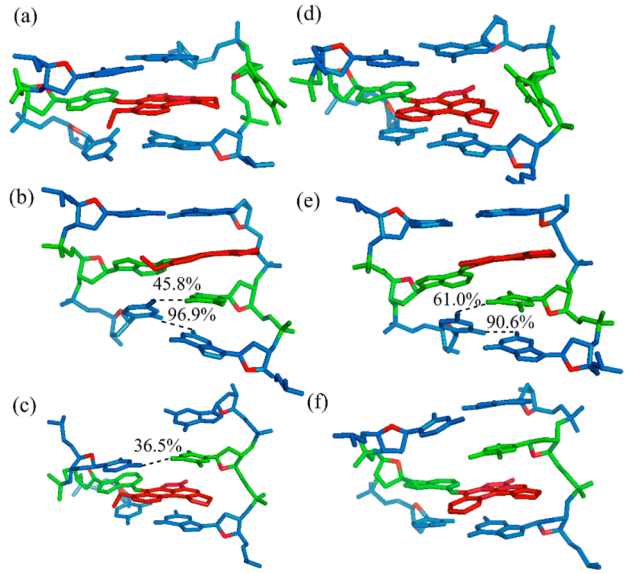

Figure 7. Representaive structures from MD simulations with the *anti* orientation of the ALI-N^6-dA (a–c) or ALII-N^6-dA (d–f) adduct paired opposite thymine in three adducted DNA conformations, namely, the base-displaced intercalated (a and d), 5′-intercalated (b and e), and 3′-intercalated (c and f) structures. Select hydrogen bond occupancies are provided (hydrogen bond distance cutoff within a 3.4 Å heavy atom separation and a 120° X–H–X angle).

the base-displaced intercalated conformer in which the damaged base is slightly displaced toward the minor groove (Figure S12 of the Supporting Information), the bulky AL moiety stacks between the 5′ and 3′ flanking base pairs (Figures 7a,d and 8a,d), and the opposing T becomes extrahelical. In the second conformation, the AL moiety stacks between the opposing T and the 5′-base with respect to the adduct in the opposite strand [denoted as 5′-intercalated (Figures 7b,e and 8b,e)]. Finally, in the third conformation, the AL moiety stacks between the opposing T and the 3′-base with respect to the adduct in the opposite strand [denoted as 3′-intercalated (Figures 7c,f and 8c,f)]. In the conformers mentioned above, the damaged adenine maintains stacking interaction with the 5′- and 3′-cytosines. Despite the symmetry of the sequence considered, the 3′- and 5′-intercalated conformations are unique because of the helical twist. The structural features of each conformation are discussed below in relation to the natural helix, where references to the 3′- and 5′-nucleotide positions of flanking bases are made with respect to the adducted nucleotide. All structural features are reported as a change with respect to the unmodified DNA sequence.

anti Base-Displaced Intercalated Conformer. In the base-displaced intercalated conformer containing the *anti* orientation of the lesion (Figure 7a,d), the bulky AL moiety intercalates into the helix. With the exception of ring I (Figure 1a), which is solvent-exposed in the major groove, all rings of the polycyclic

DOI: 10.1021/bi501484m
Biochemistry 2015, 54, 2414–2428

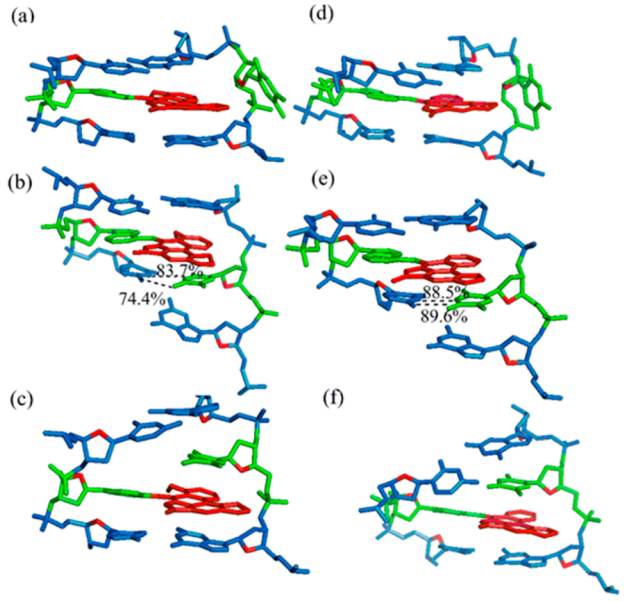

Figure 8. Representaive structures from MD simulations with the ALI-N^6-dA (a–c) or ALII-N^6-dA (d–f) adduct in the *syn* conformation paired opposite thymine in three adducted DNA conformations, namely, the base-displaced intercalated (a and d), 5′-intercalated (b and e), and 3′-intercalated (c and f) structures. Select hydrogen bond occupancies are provided (hydrogen bond distance cut off within a 3.4 Å heavy atom separation and a 120° X–H–X angle).

AL moiety are well-stacked within the helix between the 5′- and 3′-guanines in the opposing strand. Although the opposing T maintains the *anti* orientation ($\chi \sim 230–260°$), it is displaced out of the helix (Figure 7a,d). However, the flanking bases are unperturbed and maintain strong Watson–Crick (WC) hydrogen bonding [~100% occupancy (Table S33 of the Supporting Information)]. As a result, the step parameters at the lesion site change very little [shift, slide, and rise change by 1.9 Å, and the tilt, roll, and twist change by a maximum of 13° relative to those of the natural DNA (Figure 9a)]. However, there is a slight (0.4–0.5 Å) widening of the minor groove compared to that in the natural helix (Figure 9a). Nevertheless, the DNA distortions are localized to the lesion site, with minimal perturbation to the remainder of the helix.

anti 5′-Intercalated Conformer. In the 5′-intercalated conformer (Figure 7b,e), all rings of the polycyclic AL moiety (except ring I) stack within the helix between the complementary T and 5′-G in the opposing strand. Although the 5′-base pair is unperturbed [~100% occupancy (Table S33 of the Supporting Information)], C in the 3′-base pair rotates to simultaneously hydrogen bond with its complementary G and T opposing the adduct. Specifically, one [O2(C)···H–N2(G)] hydrogen bond remains in the original C:G pair for most of the simulation time [91–97% occupancy (Table S33 of the Supporting Information)], and a new sporadic interaction [N4–H(C)···O4(T)] forms between C and T [46% occupancy for ALI-N^6-dA and 61% occupancy for ALII-N^6-dA (Table S33 of the Supporting Information)]. The increase in the minor groove dimension in the 5′-intercalated conformer is greater than that observed in the base-displaced intercalated conformer (*vide supra*), which corresponds to greater untwisting of the DNA strand (Figure 9a). In addition, the shift, slide, and rise parameters increase by ~2.5 Å and the angular step parameters (tilt, roll, and twist) change by ~21° (Figure 9a). Thus, DNA is overall more distorted in this conformation than the base-displaced intercalated structure.

anti 3′-Intercalated Conformer. In the 3′-intercalated conformer, the AL moiety stacks (with ring I solvent-exposed) between the T opposing the adduct and the 3′-G in the opposing strand (Figure 7c,f). For ALI-N^6-dA, although hydrogen bonding is maintained in the 3′-flanking base pair [~100% occupancy (Table S33 of the Supporting Information)], the WC pairing of the 5′-flanking pair is disrupted. Specifically, the T opposing the adduct adopts a *syn* orientation [$\chi \sim 303°$ (Figure 7c)] and forms a N4–H(C)···O4(T) hydrogen bond with the 5′-C [36.5% occupancy (Table S33 of the Supporting Information)]. Whereas the disruption of the 5′-flanking base pair to accommodate the ALI-N^6-dA lesion widens the minor groove (~4.4 Å), the ALII-N^6-dA lesion perturbs the step parameters [e.g., the rise (Figure 9a)] at the lesion site without disrupting the WC hydrogen bonding in the flanking pairs [~100% occupancy (Table S33 of the Supporting Information)]. Thus, ALI-N^6-dA and ALII-N^6-dA adducted DNA possess slightly different structural features in the *anti* 3′-intercalated conformer.

syn Base-Displaced Intercalated Conformer. Similar to the corresponding *anti* conformation, the AL moiety intercalates

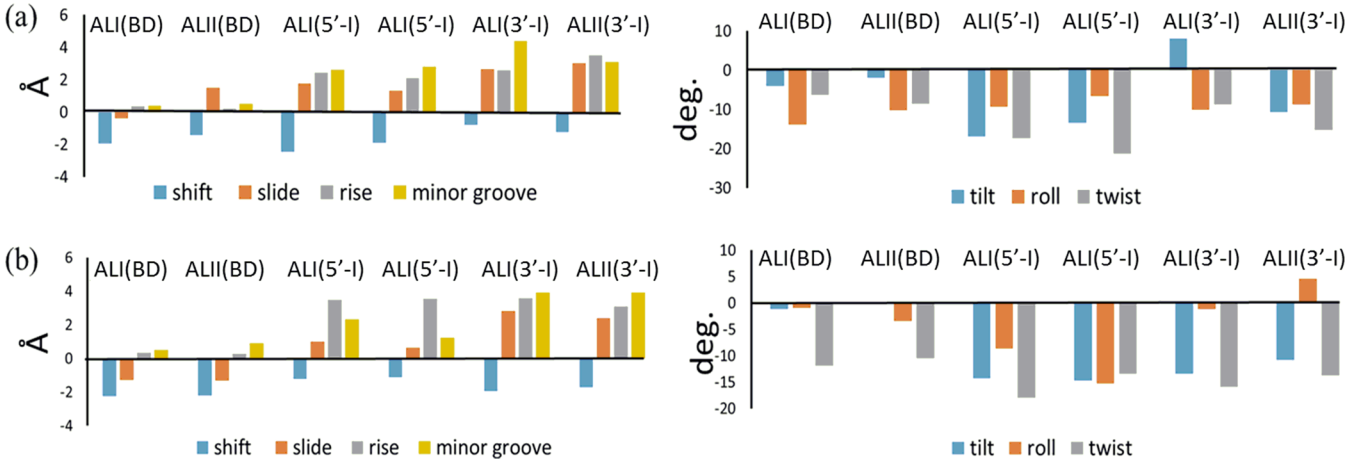

Figure 9. Change in the pseudostep parameters and minor groove dimensions relative to those of unmodified DNA for the (a) *anti* AL-N^6-dA- or (b) *syn* AL-N^6-dA adducted DNA helices in the base-displaced intercalated (BD), 5′-intercalated (5′-I), and 3′-intercalated (3′-I) conformers.

DOI: 10.1021/bi501484m
Biochemistry 2015, 54, 2414–2428

into the helix in the *syn* base-displaced intercalated conformation (Figure 8a,d), while simultaneously displacing the opposing T ($\chi \sim 210-270°$) into an extrahelical position. In contrast to the corresponding *anti* conformer, where ring I of the AL moiety is solvent-exposed, ring IV partially stacks with the flanking bases in the *syn* base-displaced conformation. However, the additional methoxy group present in ALI-N^6-dA is solvent-exposed in both the *anti* and *syn* base-displaced intercalated conformations. Regardless, the flanking bases remain unperturbed and maintain WC hydrogen bonding [~100% occupancy (Table S33 of the Supporting Information)]. As a result, the angular step parameters change by a maximum of 12° (Figure 9b), and the change in the minor groove width (0.5−0.9 Å) is almost similar to the observed widening in the corresponding *anti* conformation. The rise (~0.5 Å), shift (~2.2 Å), and slide (~0.8 Å) parameters exhibit a slightly greater perturbation than in the *anti* base-displaced intercalated conformation. Overall, the lesions are well-accommodated in DNA in the base-displaced intercalated conformation, with little perturbation to the helix.

syn 5′-Intercalated Conformer. Similar to the corresponding *anti* conformer, the AL moiety stacks between the opposing thymine and 5′-G in the opposite strand in the *syn* 5′-intercalated conformer. This intercalation moves the opposing T in the 3′-direction, which allows it to hydrogen bond with C in the 3′-base pair. In contrast to the corresponding *anti* conformer, which partially maintains a hydrogen bond in the 3′-neighboring base pair, the 3′-base pair is completely disrupted in the *syn* 5′-intercalated conformer (Figure 8b,e). Instead, two hydrogen bonds are formed between the 3′-C and T opposing the adduct, one of which [N4−H(C)···O4(T)] largely remains intact [84−90% occupancy for both adducts (Figure 8b,e)] and one [N3−H(T)···N3(C)] that is more persistent for ALII-N^6-dA (89% occupancy) than ALI-N^6-dA (75% occupancy). The complete disruption of the 3′-base pair in the *syn* 5′-intercalated conformer leads to a larger change in the rise parameter (~3.5 Å), and a narrower minor groove (~1.3−2.3 Å) relative to the natural helix than in the corresponding *anti* conformer (Figure 9b). In addition, as seen in the *syn* base-displaced intercalated conformer, ring IV of the AL moiety (Figure 1a) does not stack within the helix but rather is essentially solvent-exposed.

syn 3′-Intercalated Conformer. Similar to the corresponding *anti* conformer, the AL moiety stacks between the opposing thymine and the 3′-G in the opposing strand in the *syn* 3′-intercalated conformation (Figure 8c,f). As discussed for the *syn* 5′-intercalated structure, ring IV remains solvent-exposed. However, in contrast to the *syn* 5′-intercalated structure, WC bonding of the 5′ and 3′ flanking base pairs remains intact for both lesions [~100% occupancy (Table S33 of the Supporting Information)], as observed for the *anti* 3′-intercalated conformer of ALII-N^6-dA. To simultaneously accommodate the damaged adenine and AL moieties between the 5′- and 3′-flanking pairs, the minor groove width increases by ~4.0 Å and the rise parameter by 3.1−3.5 Å compared to those of natural DNA (Figure 9b). In fact, this minor groove widening is the largest among all three conformations with either (*anti* or *syn*) adduct orientation. In contrast, the shift and slide parameters change by a maximum of 3.5 Å and the angular step parameters by a maximum of 15° compared to those of natural DNA.

Relative Stabilities of Adducted DNA Conformers. ALI-N^6-dA Adducted DNA. The *anti* base-displaced intercalated conformer is the most energetically preferred for ALI-N^6-dA adducted DNA (Table 1) because of unperturbed WC hydrogen bonding in the flanking base pairs, as well as C−H···π interactions between ring V (Figure 1a) of the AL moiety and the extrahelical T (Figure 8a). The next most stable conformer is the *syn* base-displaced intercalated conformation, which is 2.1 kJ mol^{-1} less stable than the corresponding *anti* conformer. This energy difference is partly due to weaker stacking interactions of the damaged base and AL moiety with the 5′- and 3′-flanking base pairs [E_{vdw} (Table 1)]. The *anti* 5′-intercalated structure is the third most stable conformer, lying 36.1 kJ mol^{-1} above the global minimum (Table 1) because of disruption of WC hydrogen bonding in the 5′-flanking base pair, which is partially compensated by enhanced stacking interactions (Table 1) and additional hydrogen bonding between T opposing the adduct and the 3′-C (~46% occupancy). The *syn* 5′-intercalated conformer is ~6 kJ mol^{-1} less stable than the corresponding *anti* 5′-intercalated structure because of weaker stacking interactions, despite a higher occupancy of the 3′-C:T hydrogen bond (Figure 8b). The *syn* 3′-intercalated conformer is 49.1 kJ mol^{-1} less stable than the lowest-energy conformer but 2.3 kJ mol^{-1} more stable than the corresponding *anti* conformer. Despite weaker stacking interactions (Table 1), the *syn* 3′-intercalated conformer is more stable because of intact hydrogen bonding in both flanking base pairs, while the 5′-flanking base pair is disrupted in the *anti* conformation.

ALII-N^6-dA Adducted DNA. The *anti* base-displaced intercalated structure is energetically preferred for ALII-N^6-dA adducted DNA (Table 1) because of significant stacking stabilization and persistent WC hydrogen bonding in both flanking base pairs (Table S33 of the Supporting Information). In the absence of the methoxy group, the relative stability of the remaining conformations aligns with the stabilization provided by stacking interactions at the lesion site. Specifically, the corresponding *syn* conformer is ~8 kJ mol^{-1} less stable because of slightly weaker stacking at the lesion site, while the next most stable (*anti* and *syn* 5′-intercalated) conformations are much less stable (~34−42 kJ mol^{-1} above the global minimum)

Table 1. Relative MM-PBSA Free Energies (G_{rel}) and van der Waals Energies (E_{vdw}) for Different Conformations of AL-N^6-dA Adducted DNA Derived from 20 ns MD Simulations (in kJ mol^{-1})

adduct	orientation	conformation	G_{rel} [a]	E_{vdw} [b]
unmodified DNA	–	–	–	−70.1 ± 5.3
		base-displaced	0.0	−171.8 ± 6.8
	anti	5′-intercalated	36.1	−148.1 ± 10.9
		3′-intercalated	51.6	−148.9 ± 12.4
ALI-N^6-dA		base-displaced	2.1	−166.3 ± 7.1
	syn	5′-intercalated	42.0	−144.8 ± 10.5
		3′-intercalated	49.1	−135.6 ± 7.6
		base-displaced	0.0	−161.6 ± 6.7
	anti	5′-intercalated	33.9	−144.7 ± 11.3
		3′-intercalated	48.9	−132.1 ± 6.8
ALII-N^6-dA		base-displaced	8.0	−159.4 ± 6.3
	syn	5′-intercalated	42.7	−136.0 ± 10.5
		3′-intercalated	38.5	−127.5 ± 8.8

[a]Relative total free energy calculated with respect to the most stable comfomation for each adduct. [b]Total van der Waals interaction energy between the adducted (or natural) base present at the X^6 position in the 11-mer (Figure 1b) DNA and the flanking base pairs.

DOI: 10.1021/bi501484m
Biochemistry 2015, 54, 2414−2428

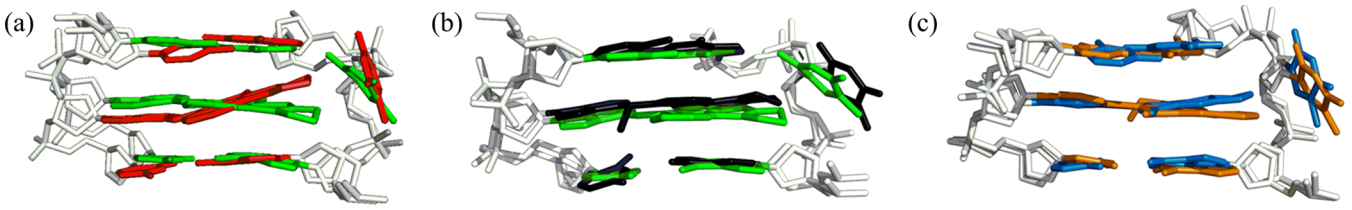

Figure 10. Trimers of base pairs containing the adducted pair comparing (a) the NMR structure[31] (red) and the representative (unrestrained) MD structure of the most stable ALII-N^6-dA adducted DNA conformation (green) (rmsd of 1.3 Å), (b) the representative (unrestrained MD) structure of the most stable *anti* conformation of ALII-N^6-dA adducted (green) and ALI-N^6-dA adducted (black) DNA (rmsd of 0.8 Å), and (c) the representative (unrestrained MD) structure of the most stable *syn* conformation of ALII-N^6-dA adducted (blue) and ALI-N^6-dA adducted (orange) DNA (rmsd of 1.0 Å).

because of significantly weaker stacking interactions. Similarly, despite intact hydrogen bonding in the 5′- and 3′-flanking base pairs, the *syn* and *anti* 3′-intercalated conformers are ∼39 and ∼49 kJ mol^{-1} less stable than the lowest-energy structure, respectively, because of weaker stacking interactions.

DISCUSSION

Conformational Heterogeneity of the AL-N^6-dA Adducts. The AL-N^6-A nucleobase models indicate that the AL and adenine moieties prefer an almost planar relative orientation in the absence of the sugar, which maximizes the number of stabilizing intramolecular hydrogen bonds. The addition of the sugar ring does not affect the orientation of the base with respect to the AL moiety, which is attached to a position far from the glycosidic bond. Although the *anti* nucleoside conformer is ∼25 kJ mol^{-1} less stable at the 5′-terminus of DNA, the *β*-constrained nucleoside and nucleotide models predict the *anti* conformer to be slightly more stable than the *syn* orientation in other helical positions (by ∼5−10 kJ mol^{-1}). This small difference in stability indicates that both the *anti* and *syn* conformations must be considered in DNA helices.

Three distinct conformations were isolated for both the *anti* and *syn* lesion orientations in ALI- and ALII-N^6-dA adducted DNA, namely, the base-displaced intercalated, 5′-intercalated, and 3′-intercalated conformers. In the base-displaced intercalated conformer, intercalation of the bulky moiety pushes the opposing T out of the helix, which disrupts the Watson−Crick hydrogen bonding between the lesion and the opposing T. This conformation parallels those presented in the literature for guanine N-linked aromatic amine adducts,[67,68] with the exception that the damaged base is displaced to a lesser extent and therefore maintains stacking interactions with the 5′- and 3′-flanking base pair in the AL-N^6-dA adducted DNA. In contrast, the 5′- and 3′-intercalated conformers of AL-N^6-dA adducted DNA parallel those previously observed for PAH adenine adducts,[20−22] where the bulky moiety intercalates into the helix between the opposing base and the base pair on the 5′- or 3′-side of the adducted pair. Because the opposing base is not displaced in the 5′- and 3′-intercalated conformers, the base step parameters are altered at the lesion site to accommodate the bulky moiety, with the degree of variation depending on both the adducted nucleotide (*anti* vs *syn*) orientation and the (5′ vs 3′) intercalation site.

Despite the range of conformations isolated from MD simulations on adducted DNA, the *anti* base-displaced intercalated conformer is the most stable and hence the most likely orientation to be adopted. Nevertheless, the *syn* base-displaced intercalated conformer is close in energy to the *anti* conformer, especially in the case of ALI-N^6-dA, indicating that a subtle change in the cellular environment may dictate the conformation of AA adducted DNA. Interestingly, the small energetic difference in the *anti*/*syn* orientation of the adducts predicted by the small (nucleoside and nucleotide) models extrapolates to adducted DNA. Nevertheless, because of greater energetic differences, other (5′- and 3′-intercalated) conformations will likely not be adopted regardless of the cellular environment. Interestingly, the higher-energy *anti*/*syn* 5′-intercalated and *syn* 3′-intercalated conformations have similar structural and energetic characteristics for both AL-N^6-dA adducts; however, the *anti* 3′-intercalated conformations of the two adducts have similar relative energies despite some structural differences at the lesion site because of the presence of select mutually compensating discrete (hydrogen-bonding and stacking) interactions involving the adduct.

Comparison to the Previous NMR Structure of ALII-N^6-dA. A recent NMR-based study of ALII-N^6-dA adducted DNA predicted an *anti* base-displaced intercalated conformation.[31] Within the same sequence, our unrestrained MD simulations isolated six stable conformers of ALII-N^6-dA adducted DNA. However, postprocessing free energy calculations reveal the same most stable (*anti* base-displaced intercalated) conformation as predicted from NMR.[31] Although complete assignments of the NOE cross-peaks were not reported in the previous NMR study,[31] lesion site structural parameters of our representative MD structure match the reported average NMR structure (Figure 10a), which dictates NOE values. Indeed, comparison of the structural parameters at the lesion site (Table S34 of the Supporting Information) indicates that the *χ* dihedral of the modified base and opposing thymine, as well as 3′-C and G, match very well between the two structures. Additionally, the sugar puckering at the T base opposing the lesion, as well as 3′-G and 5′-C, is similar to that observed from restrained MD. Furthermore, the sugar puckering of 3′-C observed using NMR is similar to the second most common sugar puckering observed in our MD simulations (Table S34 of the Supporting Information). Nevertheless, some differences in the sugar puckering of the adducted nucleotide and 5′-G are observed, and the *χ* dihedrals of the 5′-C and 5′-G bases deviate by ∼50° from the NMR value (Table S34 of the Supporting Information). In addition to the most stable conformation, our study provides information about other possible conformations for the carcinogenic AL-N^6-dA adducts. Interestingly, our calculations indicate that the *syn* base-displaced conformation, which was not derived from the NMR data of ALII-N^6-dA adducted DNA, may also be energetically accessible with slight perturbations to the surrounding environment (e.g., within the active site of lesion-bypass polymerases).[69]

DOI: 10.1021/bi501484m
Biochemistry 2015, 54, 2414−2428

Comparison of the ALI-N^6-dA and ALII-N^6-dA Adducts. Although NMR data are available for ALII-N^6-dA, no such structural study has been conducted for ALI-N^6-dA. Nevertheless, the close agreement between our most stable conformation of ALII adducted DNA and the one determined on the basis of NMR[31] suggests that reliable information can be obtained from our MD data. Free energy calculations indicate that the most stable conformation is the *anti* base-displaced intercalated structure for both ALI-N^6-dA and ALII-N^6-dA adducted DNA. Furthermore, an overlay of the representative structures for both adducts indicates these conformers are very similar (Figure 10b). Both adducts can also lead to the *syn* base-displaced intercalated conformation of adducted DNA. However, the *syn* base-displaced intercalated conformer is associated with a greater energetic penalty in the case of the ALII-N^6-dA (8.0 kJ mol^{-1}) than in the case of the ALI-N^6-dA (2.1 kJ mol^{-1}). Interestingly, when the lesion site van der Waals energy is calculated over the simulation trajectories of ALI-N^6-dA adducted DNA with the methoxy group removed, the methoxy group is determined to increase the van der Waals energies equally (by ∼10 kJ mol^{-1}) in the *anti* and *syn* base-displaced intercalated conformations (Table S35 of the Supporting Information). Thus, the smaller energy difference between the *anti* and *syn* base-displaced intercalated conformations for ALI-N^6-dA compared to that for ALII-N^6-dA does not directly arise because of van der Waals interactions involving the methoxy group. Instead, the methoxy group exerts a spatial effect only in the *anti* base-displaced intercalated conformation, which is most significantly reflected in the displacement of the AL moiety relative to ALII-N^6-dA (see overlays in Figure S13 of the Supporting Information). The synergistic effect of several geometric changes is ultimately one factor that alters the stability of the *anti* base-displaced intercalated conformation relative to the *syn* counterpart. In addition, the *syn* base-displaced intercalated conformations are more hydrated, and therefore, the location of the bulky moiety is more stabilized than the *anti* orientation for both ALI-N^6-dA and ALII-N^6-dA (Figure 11). However, the difference in hydration is greater for ALI-N^6-dA, which further reduces the *anti*/*syn* energy difference.

The greater energetic difference between the *anti* and *syn* base-displaced intercalated conformers for ALII-N^6-dA may explain why a detectable fraction of the *syn* base-displaced intercalated conformer was not observed in the previous NMR study.[31] In contrast, the relative energies suggest that the fraction of the *syn* base-displaced intercalated conformation may be greater for ALI-N^6-dA adducted DNA. Indeed, our calculations indicate that this conformation may be detectable in NMR experiments and therefore will likely play an important role in determining the mutagenic potential of the ALI-N^6-dA adduct. Although the mutagenic activity of the lesion is dependent on the adduct conformation at the single strand–double strand junction[70] and the active site of polymerases,[71,72] the intrinsic adduct conformation of adducted double-stranded DNA (dsDNA) in solution has been shown to persist in the polymerase active site for select PAH and aromatic amine adducts.[73] Furthermore, a greater flexibility in the active site of a lesion-bypass polymerase has been associated with an increased level of misincorporation upon replication.[74] Therefore, if the smaller energetic difference between the *syn* and *anti* base-displaced intercalated conformations for ALI-N^6-dA than ALII-N^6-dA adducted DNA persists in the polymerase, then the ALI-N^6-dA adduct will likely have a stronger tendency to induce base mismatches. This proposal correlates with the experimentally observed greater mutagenic potential of ALI-N^6-dA over ALII-N^6-dA.[32,34]

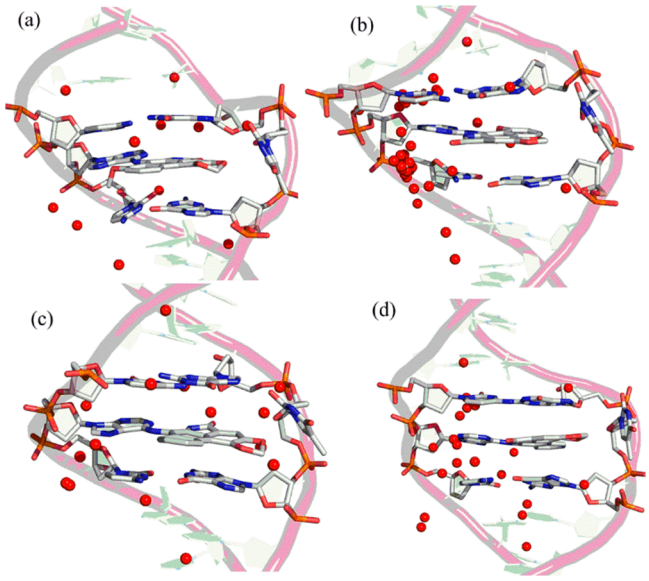

Figure 11. Hydration pattern surrounding the structures of *anti* (a and c) and *syn* (b and d) base-displaced intercalated conformers of ALI-N^6-dA (a and b) and ALII-N^6-dA (c and d) adducted DNA. The water molecules within 5 Å of the lesion for more than 80% of the simulation time are shown (red spheres).

DNA adducts that are structurally similar but differ in the chemical composition of the bulky group via stereochemistry[20] or the presence of additional rings[75,76] display different conformational preferences. However, the ALI-N^6-dA and ALII-N^6-dA adducts provide only the second example of lesions that potentially exhibit unique conformational outcomes and chemically differ by a substituent. Specifically, the compositions of AAF (acetylaminoflourene) and AF (aminoflourene) deviate by an acetyl substituent on the N-linkage and lead to three conformations for AAF-dG adducted DNA (namely, major groove, base-displaced stacked, and minor-groove wedge) versus two conformations of AF-dG adducted DNA (namely, major groove and base-displaced stacked).[77] This difference occurs because steric repulsion involving the attached acetyl group causes the damaged guanine to become nonplanar, which diminishes the stacking energy at the lesion site compared to that of (a nearly coplanar) AF-dG.[77] In the case of the ALI and ALII-N^6-dA adducts, the distinguishing methoxy substituent is located on the bulky ring rather than the linkage and therefore does not sterically interact with the damaged base. Nevertheless, these adducts exhibit diverse conformational flexibility because the additional methoxy group in ALI-N^6-dA changes the relative geometries and hydration of the *syn* and *anti* base-displaced intercalated conformers at the lesion site. This example further underscores that subtle changes in the chemical composition of bulky adducts can affect the conformational equilibrium of the associated dsDNA.

Comparison to Other N^6-Linked dA Adducts. A number of other carcinogens form adducts at the N6 site of dA, which can broadly be divided into two main categories: (i) adducts lacking a conjugated π-ring (e.g., DHB-dA[78] formed from 1,3-butadiene, and endogenous estrogen adducts, including 2-OHE$_1$-6α-N^6-dA and 2-OHE$_1$-6β-N^6-dA[79]) and (ii) adducts containing a conjugated polycyclic π-system (e.g., PAH

DOI: 10.1021/bi501484m
Biochemistry 2015, 54, 2414−2428

adducts).[20−22,24,25,28,29,80] Adducts that lack conjugated π-rings prefer non-intercalated conformations with the bulky moiety in either the minor or major groove.[78,79] On the other hand, N^6-dA adducts with polycyclic π-systems preferentially form intercalated conformations that are stabilized through π-π interactions between the bulky moiety and the flanking bases in the DNA helix.[37,50,52,58,59,62,63,70]

Similar to PAH adducts, the AA lesions contain a conjugated π-ring, and the associated adducted DNA preferentially adopts an intercalated conformation. However, the AL-N^6-dA adducts preferentially induce a base-displaced intercalated conformation, while most PAH adducts lead to either the 5′- or 3′-intercalated conformation. Furthermore, although the preferred intercalated structures associated with PAH adducts either partially or completely maintain Watson−Crick hydrogen bonding in the damaged base pair,[20−22,24] the hydrogen bonding in the lesion pair is entirely disrupted in all conformations of AL-N^6-dA adducted DNA. This variance arises because of differences in the conjugation of the carbon atom in the bulky moiety attached to N6 of adenine. Specifically, the AL adducts adopt a planar orientation of the bulky moiety with respect to the base due to extended conjugation of N6 in A with an sp^2 hybridized carbon in the AL moiety, while the carbon attached to N6 in A is sp^3 hybridized in the PAH adducts.[81] The absence of extended conjugation and intramolecular hydrogen bonding imparts flexibility to the PAH lesions that allows the bulky moiety to bend and maintain hydrogen bonding with the opposing base upon intercalation.

Interestingly, the preferred DNA conformations of AL-N^6-dA are less structurally distorting than conformations of DNA containing PAH adducts. In the preferred base-displaced intercalated conformations of AL-N^6-dA adducted DNA, the lesion causes minimal changes to the pseudostep parameters and the minor groove width. In contrast, in the 5′- or 3′-intercalated conformations, the PAH adducts significantly change the pseudostep parameters and the minor groove width of natural DNA.[20,82] Although energetically inaccessible (5′-intercalated and 3′-intercalated) conformations of ALI-N^6-dA- and ALII-N^6-dA adducted DNA exhibit greater helical distortions, these conformers are still less distorted than the PAH-induced conformations. Thus, the planar conformations of the AL-N^6-dA adducts are better accommodated in DNA than the nonplanar PAH adducts.

NER Recognition of AA Adducts. Previous studies based on ^{32}P postlabeling assays have revealed that ALI-N^6-dA is more persistent in cells than ALII-N^6-dA.[32,33] However, it is currently unclear whether this difference arises because of differences in the repair propensity of the two lesions. Bulky DNA lesions are generally repaired by the nucleotide excision repair (NER) pathway, which removes a short segment (∼24−32 nucleotides) of the lesion-containing DNA strand.[83] One of the most versatile mechanisms for NER of bulky lesions is the global genomic repair (GGR) pathway, which involves recognition factors (e.g., XPC-RAD23B in eukaryotes) that constantly scan the genome. Studies of other bulky adducts (mainly the PAH and aromatic amine purine adducts) have shown that the damage is typically recognized in the GGR pathway by thermodynamic destabilization induced by the lesion.[84−87] Changes in the thermodynamic stability have been directly connected to alterations in structural features such as distortion to the helix at the lesion site,[86,88−90] an increase in helical[91] and backbone[90] dynamics, enhanced stacking interactions involving the damaged base,[92,93] and the identity of the partner base.[94] On the other hand, the transcription-coupled repair (TCR) pathway of NER is more efficient in transcriptionally active regions of the genome, where lesion-induced stalling of RNA polymerases serves as the lesion recognition signal.[95]

Previous studies have shown that the ALII-N^6-dA adduct is resistant to GGR and is exclusively repaired by the TCR pathway.[14] Our calculations may provide the currently missing structural explanations for the resistance of the ALII-N^6-dA adducts to GGR and the greater relative persistence of ALI-N^6-dA. First, close examination of the preferred (*anti* base-displaced intercalated) conformations of both AL-N^6-dA adducts indicates that the displacement of the opposing thymine into the major groove results in the loss of stacking interactions with the flanking base pairs compared to the natural helix. However, this destabilization is effectively compensated by additional stacking stabilization between the AL moiety and the flanking base pairs at the lesion site (Table 1). In fact, stacking interactions are enhanced in all conformations of AL adducted DNA compared to the natural helix (Table 1). Second, distortions in the base step parameters relative to those of the natural helix for both adducts indicate that these planar DNA lesions do not substantially distort DNA, which may prevent the GGR recognition step. Third, the dynamics of both modified DNA strands are similar to the natural strand (Figure S14 of the Supporting Information). Therefore, the enhanced stacking, lack of helical distortion, and minimal changes in helical dynamics relative to those of the natural helix together might explain the resistance of these lesions to GGR.

In addition to the factors described above, a previous crystal structure of the yeast orthologue of the initial GGR recognition factor (XPC-RAD23B) by Min et al.[85] reveals that the initial steps in lesion recognition involve insertion of a β-hairpin via the major groove side of DNA and flipping of the lesion and opposing base(s) out of the helix into the DNA minor groove. Because the AL-N^6-dA adducts intercalate via the major groove in the most stable *anti* base-displaced intercalated structure, these conformers may obstruct insertion of a β-hairpin into DNA. In addition, displacement of the opposing T into the major groove in the most stable conformation could block interactions between the enzyme and the lesion site in DNA. Thus, as indicated for PAH-N^6-dA lesions,[84] unfavorable steric interactions between the lesion intercalating through the DNA major groove and the β-hairpin of the XPC-RAD23B recognition factor may also prevent the AL-N^6-dA lesions from being effectively recognized by GGR.

Most importantly, the factors that potentially affect the repair propensities (e.g., stacking energies, distortions at the lesion site, helical dynamics, and the helical position of the AL moiety) are very similar for DNA containing ALII-N^6-dA and ALI-N^6-dA. Therefore, it is likely that both lesions are equally resistant to the GGR pathway. This implies that the greater persistence of ALI-N^6-dA in cells is not because of differential repair propensities but rather must be due to other factors, such as the experimentally observed greater activation and binding of AAI than AAII to DNA.[16]

■ CONCLUSIONS

The intrinsic flexibility of the AL-N^6-dA adducts about the glycosidic bond holds true both in the nucleoside/nucleotide units and within DNA, which suggests that small computational models can provide important insights into the conformational

DOI: 10.1021/bi501484m
Biochemistry 2015, 54, 2414−2428

preference of DNA adducts. Unrestrained MD simulations predict the *anti* base-displaced intercalated conformation of adducted DNA to be the most stable, which agrees with previously published NMR data for ALII-N^6-dA adducted DNA and thereby validates our methodology. Using the same approach, structural information for the more prevalent ALI-N^6-dA adduct was obtained for the first time. Most importantly, free energy calculations reveal that the ALI-N^6-dA adduct possesses greater *anti*/*syn* conformational flexibility. If this increased flexibility persists in the active site of lesion-bypass polymerases, this may explain the experimentally observed greater nephrotoxic potential of the ALI-N^6-dA adduct over that of the ALII-N^6-dA adduct.[34] Furthermore, our work provides structural clues for the NER resistance of both AA adenine adducts, including enhanced stacking, lack of helical distortions, and minimal changes in helical dynamics relative to those of natural DNA, as well as possible blockage of β-hairpin insertion of the GGR recognition factor. Nevertheless, further computational and experimental work is required to analyze the *anti*/*syn* barriers to rotation about the glycosidic bond in dsDNA, which will provide further insight into the flexibility of the adducted DNA and thereby serve as an important tool for deducing conformational outcomes. Furthermore, additional biochemical studies of the conformations of the AL-N^6-dA adducts within the active sites of NER and replication enzymes are required to evaluate our hypotheses based on the preferred conformations of dsDNA.

■ ASSOCIATED CONTENT

Supporting Information

χ scan for natural and modified adenine (Figure S1); backbone rmsd versus time in all adducted DNA conformations (Figure S2); the distribution of twist angles for the pseudostep obtained from the 20 and 320 ns simulations (Figure S3); Radar plots for the probability distribution of χ, θ, and ϕ for all adducted DNA conformations (Figures S4−S7); fully optimized B3LYP-D3 nucleoside minima with different ϕ values (Figures S8−S11); overlay of the trimers containing the 5′- and 3′-flanking base pairs of the modified strand and the natural strand showing the displacement of the modified adenine (Figure S12); overlay of the damaged base in the base-displaced intercalated conformers in the *anti* and *syn* orientations of the adducts (Figure S13); pseudostep parameters and minor groove dimensions for ALI-N^6-dA and ALII-N^6-dA adducted DNA (Figure S14); comparison of B3LYP and B3LYP-D3 structural parameters for the nucleobase and nucleoside adducts (Tables S1−S3); Cartesian coordinates of minima for all DFT models (Tables S4−S27); volume of the 8 Å water box and the number of water residues and sodium ions added in each simulation (Table S28); Mol2 file of the nucleotide adducts generated using the RED program (Tables S29 and S30); χ distribution obtained from MD simulations and the χ value in QM nucleoside models (Table S31); comparison of the pseudostep parameters and minor groove dimensions for ALI-N^6-dA and ALII-N^6-dA adducted DNA, as well as the natural strand, from 20 and 320 ns simulations (Table S32); hydrogen-bonding occupancies in the trimers composed of the damaged base pair and the 3′- and 5′-flanking bases (Table S33); comparison of structural parameters for DNA containing ALII-N^6-dA obtained from NMR and the most stable base-displaced intercalated conformation obtained from MD simulations (Table S34); and effect of the methoxy group on the van der Waals interaction energy between the adducted base and the flanking base pairs for DNA containing ALI-N^6-dA in the *syn* and *anti* base-displaced intercalated conformers (Table S35). This material is available free of charge via the Internet at http://pubs.acs.org.

■ AUTHOR INFORMATION

Corresponding Author

*E-mail: stacey.wetmore@uleth.ca. Telephone: (403) 329-2323. Fax: (403) 329-2057.

Funding

Support for this research was provided by the Canada Foundation for Innovation (CFI), the Natural Sciences and Engineering Research Council (NSERC) of Canada, the Canada Research Chair (CRC) program, and the University of Lethbridge Research Fund. P.K. thanks the University of Lethbridge for financial support.

Notes

The authors declare no competing financial interest.

■ ACKNOWLEDGMENTS

Calculations were conducted on the Up-scale and Robust Abacus for Chemistry in Lethbridge (URACIL) and the New Up-scale Cluster for Lethbridge to Enable Innovative Chemistry (NUCLEIC). Additional computational resources were provided by WestGrid and Compute/Calcul Canada.

■ ABBREVIATIONS

dA, 2′-deoxyadenosine; dG, 2′-deoxyguanosine; MD, molecular dynamics; AA, aristolochic acid; AL, aristolactam; ALII-N^6-dA, aristolactam II-dA adduct; ALI-N^6-dA, aristolactam I-dA adduct; rmsd, root mean square deviation; QM, quantum mechanical; DFT, density functional theory; AAF-dG, acetylaminofluorene-dG adduct; AF-dG, aminofluorene-dG adduct; PAH, polycyclic aromatic hydrocarbons; OTB-dG, C-linked ochratoxin A-dG adduct; PhOH-dG, phenoxl-dG adduct; GAFF, general AMBER force field; PES, potential energy surface; IARC, International Agency for Research on Cancer; NER, nucleotide excision repair; GGR, global genomic repair; TCR, transcription-coupled repair.

■ REFERENCES

(1) Vanherweghem, J. L., Tielemans, C., Abramowicz, D., Depierreux, M., Vanhaelen-Fastre, R., Vanhaelen, M., Dratwa, M., Richard, C., Vandervelde, D., Verbeelen, D., and Jadoul, M. (1993) Rapidly progressive interstitial renal fibrosis in young women: Association with slimming regimen including Chinese herbs. *Lancet 341*, 387−391.

(2) Ivić, M. (1969) Etiology of endemic nephropathy. *Lijec. Vjesn. 91*, 1273.

(3) Djukanović, L., and Radovanović, Z. (2003) Balkan endemic nephropathy. In *Clinical Nephrotoxins* (de Broe, M., Porter, G., Bennett, W., and Verpooten, G., Eds.) pp 587−601, Springer, Dordeecht, The Netherlands.

(4) De Broe, M. E. (2012) Chinese herbs nephropathy and Balkan endemic nephropathy: Toward a single entity, aristolochic acid nephropathy. *Kidney Int. 81*, 513−515.

(5) Arlt, V. M., Stiborová, M., vom Brocke, J., Simões, M. L., Lord, G. M., Nortier, J. L., Hollstein, M., Phillips, D. H., and Schmeiser, H. H. (2007) Aristolochic acid mutagenesis: Molecular clues to the aetiology of Balkan endemic nephropathy-associated urothelial cancer. *Carcinogenesis 28*, 2253−2261.

(6) Chen, C.-H., Dickman, K. G., Moriya, M., Zavadil, J., Sidorenko, V. S., Edwards, K. L., Gnatenko, D. V., Wu, L., Turesky, R. J., Wu, X.-R., Pu, Y.-S., and Grollman, A. P. (2012) Aristolochic acid-associated urothelial cancer in Taiwan. *Proc. Natl. Acad. Sci. U.S.A. 109*, 8241−8246.

DOI: 10.1021/bi501484m
Biochemistry 2015, 54, 2414−2428

(7) Cosyns, J.-P., Jadoul, M., Squifflet, J.-P., Wese, F.-X., and van Ypersele de Strihou, C. (1999) Urothelial lesions in Chinese-herb nephropathy. *Am. J. Kidney Dis. 33*, 1011−1017.
(8) *IARC monographs-100 A Plants containing aristolochic acids* (2002) 347−361, International Agency for Research on Cancer, Lyon, France.
(9) Attaluri, S., Bonala, R. R., Yang, I.-Y., Lukin, M. A., Wen, Y., Grollman, A. P., Moriya, M., Iden, C. R., and Johnson, F. (2010) DNA adducts of aristolochic acid II: Total synthesis and site-specific mutagenesis studies in mammalian cells. *Nucleic Acids Res. 38*, 339−352.
(10) Grollman, A. P., Shibutani, S., Moriya, M., Miller, F., Wu, L., Moll, U., Suzuki, N., Fernandes, A., Rosenquist, T., Medverec, Z., Jakovina, K., Brdar, B., Slade, N., Turesky, R. J., Goodenough, A. K., Rieger, R., Vukelić, M., and Jelaković, B. (2007) Aristolochic acid and the etiology of endemic (Balkan) nephropathy. *Proc. Natl. Acad. Sci. U.S.A. 104*, 12129−12134.
(11) Hoang, M. L., Chen, C.-H., Sidorenko, V. S., He, J., Dickman, K. G., Yun, B. H., Moriya, M., Niknafs, N., Douville, C., Karchin, R., Turesky, R. J., Pu, Y.-S., Vogelstein, B., Papadopoulos, N., Grollman, A. P., Kinzler, K. W., and Rosenquist, T. A. (2013) Mutational Signature of Aristolochic Acid Exposure as Revealed by Whole-Exome Sequencing. *Sci. Transl. Med. 5*, 197ra102.
(12) Hranjec, T., Kovac, A., Kos, J., Mao, W. Y., Chen, J. J., Grollman, A. P., and Jelakovic, B. (2005) Endemic nephropathy: The case for chronic poisoning by Aristolochia. *Croat. Med. J. 46*, 116−125.
(13) Sidorenko, V. S., Attaluri, S., Zaitseva, I., Iden, C. R., Dickman, K. G., Johnson, F., and Grollman, A. P. (2014) Bioactivation of the human carcinogen aristolochic acid. *Carcinogenesis 35*, 1814−1822.
(14) Sidorenko, V. S., Yeo, J.-E., Bonala, R. R., Johnson, F., Schärer, O. D., and Grollman, A. P. (2012) Lack of recognition by global-genome nucleotide excision repair accounts for the high mutagenicity and persistence of aristolactam-DNA adducts. *Nucleic Acids Res. 40*, 2494−2505.
(15) Stiborová, M., Mareîs, J., Frei, E., Arlt, V. M., Martínek, V., and Schmeiser, H. H. (2011) The human carcinogen aristolochic acid I is activated to form DNA adducts by human NAD(P)H:quinone oxidoreductase without the contribution of acetyltransferases or sulfotransferases. *Environ. Mol. Mutagen. 52*, 448−459.
(16) Martinek, V., Kubickova, B., Arlt, V. M., Frei, E., Schmeiser, H. H., Hudecek, J., and Stiborova, M. (2010) Comparison of activation of aristolochic acid I and II with NADPH:quinone oxidoreductase, sulphotransferases and N-acetyltranferases. *Neuroendocrinol. Lett. 32*, 57−70.
(17) Schmeiser, H. H., Frei, E., Wiessler, M., and Stiborova, M. (1997) Comparison of DNA adduct formation by aristolochic acids in various in vitro activation systems by ^{32}P-post-labelling: Evidence for reductive activation by peroxidases. *Carcinogenesis 18*, 1055−1062.
(18) Moriya, M., Slade, N., Brdar, B., Medverec, Z., Tomic, K., Jelaković, B., Wu, L., Truong, S., Fernandes, A., and Grollman, A. P. (2011) TP53 mutational signature for aristolochic acid: An environmental carcinogen. *Int. J. Cancer 129*, 1532−1536.
(19) Poon, S. L., Pang, S.-T., McPherson, J. R., Yu, W., Huang, K. K., Guan, P., Weng, W.-H., Siew, E. Y., Liu, Y., Heng, H. L., Chong, S. C., Gan, A., Tay, S. T., Lim, W. K., Cutcutache, I., Huang, D., Ler, L. D., Nairismägi, M.-L., Lee, M. H., Chang, Y.-H., Yu, K.-J., Chan-on, W., Li, B.-K., Yuan, Y.-F., Qian, C.-N., Ng, K.-F., Wu, C.-F., Hsu, C.-L., Bunte, R. M., Stratton, M. R., Futreal, P. A., Sung, W.-K., Chuang, C.-K., Ong, C. K., Rozen, S. G., Tan, P., and Teh, B. T. (2013) Genome-Wide Mutational Signatures of Aristolochic Acid and Its Application as a Screening Tool. *Sci. Transl. Med. 5*, 197ra101.
(20) Cai, Y., Ding, S., Geacintov, N. E., and Broyde, S. (2011) Intercalative Conformations of the 14R (+)- and 14S (−)-trans-anti-DB a,l P-N-6-dA Adducts: Molecular Modeling and MD Simulations. *Chem. Res. Toxicol. 24*, 522−531.
(21) Li, Z., Kim, H.-Y., Tamura, P. J., Harris, C. M., Harris, T. M., and Stone, M. P. (1999) Intercalation of the (1S,2R,3S,4R)-N6-[1-(1,2,3,4-Tetrahydro-2,3,4-trihydroxybenz[a]anthracenyl)]-2′-deoxyadenosyl Adduct in an Oligodeoxynucleotide Containing the Human N-ras Codon 61 Sequence. *Biochemistry 38*, 16045−16057.
(22) Li, Z., Mao, H., Kim, H.-Y., Tamura, P. J., Harris, C. M., Harris, T. M., and Stone, M. P. (1999) Intercalation of the (−)-(1R,2S,3R,4S)-N6-[1-Benz[a]anthracenyl]-2′-deoxyadenosyl Adduct in an Oligodeoxynucleotide Containing the Human N-ras Codon 61 Sequence. *Biochemistry 38*, 2969−2981.
(23) Li, Z., Tamura, P. J., Wilkinson, A. S., Harris, C. M., Harris, T. M., and Stone, M. P. (2001) Intercalation of the (1R,2S,3R,4S)-N6-[1-(1,2,3,4-Tetrahydro-2,3,4-trihydroxybenz[a]anthracenyl)]-2′-deoxyadenosyl Adduct in the N-ras Codon 61 Sequence: DNA Sequence Effects. *Biochemistry 40*, 6743−6755.
(24) Mao, B., Gu, Z., Gorin, A., Chen, J., Hingerty, B. E., Amin, S., Broyde, S., Geacintov, N. E., and Patel, D. J. (1999) Solution Structure of the (+)-cis-anti-Benzo[a]pyrene-dA ([BP]dA) Adduct Opposite dT in a DNA Duplex. *Biochemistry 38*, 10831−10842.
(25) Kropachev, K., Kolbanovskiy, M., Liu, Z., Cai, Y., Zhang, L., Schwaid, A. G., Kolbanovskiy, A., Ding, S., Amin, S., Broyde, S., and Geacintov, N. E. (2013) Adenine−DNA Adducts Derived from the Highly Tumorigenic Dibenzo[a,l]pyrene Are Resistant to Nucleotide Excision Repair while Guanine Adducts Are Not. *Chem. Res. Toxicol. 26*, 783−793.
(26) Volk, D. E., Rice, J. S., Luxon, B. A., Yeh, H. J. C., Liang, C., Xie, G., Sayer, J. M., Jerina, D. M., and Gorenstein, D. G. (2000) NMR Evidence for Syn-Anti Interconversion of a Trans Opened (10R)-dA Adduct of Benzo[a]pyrene (7S,8R)-Diol (9R,10S)-Epoxide in a DNA Duplex. *Biochemistry 39*, 14040−14053.
(27) Le, P. T. Q., Harris, C. M., Harris, T. M., and Stone, M. P. (2000) Altered Electrophoretic Migration of Polycyclic Aromatic Hydrocarbon and Styrene Oxide Adducts at Adenine N6 Correlates with Adduct-Induced Structural Disorder. *Chem. Res. Toxicol. 13*, 63−71.
(28) Zegar, I. S., Kim, S. J., Johansen, T. N., Horton, P. J., Harris, C. M., Harris, T. M., and Stone, M. P. (1996) Adduction of the Human N-ras Codon 61 Sequence with (−)-(7S,8R,9R,10S)-7,8-Dihydroxy-9,10-epoxy-7,8,9,10-tetrahydrobenzo[a]pyrene: Structural Refinement of the Intercalated SRSR(61,2) (−)-(7S,8R,9S,10R)-N6-[10-(7,8,9,10-Tetrahydrobenzo[a]pyrenyl)]-2′-deoxyadenosyl Adduct from ^{1}H NMR. *Biochemistry 35*, 6212−6224.
(29) Zegar, I. S., Chary, P., Jabil, R. J., Tamura, P. J., Johansen, T. N., Lloyd, R. S., Harris, C. M., Harris, T. M., and Stone, M. P. (1998) Multiple Conformations of an Intercalated (−)-(7S,8R,9S,10R)-N6-[10-(7,8,9,10-Tetrahydrobenzo[a]pyrenyl)]-2′-deoxyadenosyl Adduct in the N-ras Codon 61 Sequence. *Biochemistry 37*, 16516−16528.
(30) Geacintov, N. E., Cosman, M., Hingerty, B. E., Amin, S., Broyde, S., and Patel, D. J. (1997) NMR Solution Structures of Stereoisomeric Covalent Polycyclic Aromatic Carcinogen−DNA Adducts: Principles, Patterns, and Diversity. *Chem. Res. Toxicol. 10*, 111−146.
(31) Lukin, M., Zaliznyak, T., Johnson, F., and de los Santos, C. (2012) Structure and stability of DNA containing an aristolactam II-dA lesion: Implications for the NER recognition of bulky adducts. *Nucleic Acids Res. 40*, 2759−2770.
(32) Bieler, C. A., Stiborova, M., Wiessler, M., Cosyns, J. P., van Ypersele de Strihou, C., and Schmeiser, H. H. (1997) ^{32}P-post-labelling analysis of DNA adducts formed by aristolochic acid in tissues from patients with Chinese herbs nephropathy. *Carcinogenesis 18*, 1063−1067.
(33) Pfau, W., Schmeiser, H. H., and Wiessler, M. (1990) ^{32}P-Postlabelling analysis of the DNA adducts formed by aristolochic acid I and II. *Carcinogenesis 11*, 1627−1633.
(34) Shibutani, S., Dong, H., Suzuki, N., Ueda, S., Miller, F., and Grollman, A. P. (2007) Selective Toxicity of Aristolochic Acids I and II. *Drug Metab. Dispos. 35*, 1217−1222.
(35) Milhé, C., Dhalluin, C., Fuchs, R. P. P., and Lefèvre, F.-F. (1994) NMR evidence of the stabilisation by the carcinogen N-2-acetylaminofluorene of a frameshift mutagenesis intermediate. *Nucleic Acids Res. 22*, 4646−4652.
(36) Norman, D., Abuaf, P., Hingerty, B. E., Live, D., Grunberger, D., Broyde, S., and Patel, D. J. (1989) NMR and computational characterization of the N-(deoxyguanosin-8-yl)aminofluorene adduct

DOI: 10.1021/bi501484m
Biochemistry 2015, 54, 2414−2428

[(AF)G] opposite adenosine in DNA: (AF)G[syn]·A[anti] pair formation and its pH dependence. *Biochemistry 28*, 7462−7476.
(37) Tan, X., Suzuki, N., Grollman, A. P., and Shibutani, S. (2002) Mutagenic Events in *Escherichia coli* and Mammalian Cells Generated in Response to Acetylaminofluorene-Derived DNA Adducts Positioned in the NarI Restriction Enzyme Site. *Biochemistry 41*, 14255−14262.
(38) Patel, D. J., Mao, B., Gu, Z., Hingerty, B. E., Gorin, A., Basu, A. K., and Broyde, S. (1998) Nuclear Magnetic Resonance Solution Structures of Covalent Aromatic Amine−DNA Adducts and Their Mutagenic Relevance. *Chem. Res. Toxicol. 11*, 391−407.
(39) Schorr, S., and Carell, T. (2010) Mechanism of Acetylaminofluorene-dG Induced Frameshifting by Polymerase *η*. *ChemBioChem 11*, 2534−2537.
(40) Milhe, C., Fuchs, R. P. P., and Lefevre, J. F. (1996) NMR data show that the carcinogen N-2-acetylaminofluorene stabilises an intermediate of −2 frameshift mutagenesis in a region of high mutation frequency. *Eur. J. Biochem. 235*, 120−127.
(41) Pfau, W., Schmeiser, H. H., and Wiessler, M. (1991) N6-Adenyl arylation of DNA by aristolochic acid II and a synthetic model for the putative proximate carcinogen. *Chem. Res. Toxicol. 4*, 581−586.
(42) Zgarbová, M., Luque, F. J., Šponer, J., Cheatham, T. E., Otyepka, M., and Jurečka, P. (2013) Toward Improved Description of DNA Backbone: Revisiting *ε* and *ζ* Torsion Force Field Parameters. *J. Chem. Theory Comput. 9*, 2339−2354.
(43) Millen, A. L., Manderville, R. A., and Wetmore, S. D. (2010) Conformational Flexibility of C8-Phenoxyl-2′-deoxyguanosine Nucleotide Adducts. *J. Phys. Chem. B 114*, 4373−4382.
(44) Frisch, M. J., Trucks, G. W., Schlegel, H. B., Scuseria, G. E., Robb, M. A., Cheeseman, J. R., Scalmani, G., Barone, V., Mennucci, B., Petersson, G. A., Nakatsuji, H., Caricato, M., Li, X., Hratchian, H. P., Izmaylov, A. F., Bloino, J., Zheng, G., Sonnenberg, J. L., Hada, M., Ehara, M., Toyota, K., Fukuda, R., Hasegawa, J., Ishida, M., Nakajima, T., Honda, Y., Kitao, O., Nakai, H., Vreven, T., Montgomery, J. A., Jr., Peralta, J. E., Ogliaro, F., Bearpark, M., Heyd, J. J., Brothers, E., Kudin, K. N., Staroverov, V. N., Keith, T., Kobayashi, R., Normand, J., Raghavachari, K., Rendell, A., Burant, J. C., Iyengar, S. S., Tomasi, J., Cossi, M., Rega, N., Millam, J. M., Klene, M., Knox, J. E., Cross, J. B., Bakken, V., Adamo, C., Jaramillo, J., Gomperts, R., Stratmann, R. E., Yazyev, O., Austin, A. J., Cammi, R., Pomelli, C., Ochterski, J. W., Martin, R. L., Morokuma, K., Zakrzewski, V. G., Voth, G. A., Salvador, P., Dannenberg, J. J., Dapprich, S., Daniels, A. D., Farkas, O., Foresman, J. B., Ortiz, J. V., Cioslowski, J., and Fox, D. J. (2010) *Gaussian 09*, revision C.01, Gaussian, Inc., Wallingford, CT.
(45) Frisch, M. J., Trucks, G. W., Schlegel, H. B., Scuseria, G. E., Robb, M. A., Cheeseman, J. R., Scalmani, G., Barone, V., Mennucci, B., Petersson, G. A., Nakatsuji, H., Caricato, M., Li, X., Hratchian, H. P., Izmaylov, A. F., Bloino, J., Zheng, G., Sonnenberg, J. L., Hada, M., Ehara, M., Toyota, K., Fukuda, R., Hasegawa, J., Ishida, M., Nakajima, T., Honda, Y., Kitao, O., Nakai, H., Vreven, T., Montgomery, J. A., Jr., Peralta, J. E., Ogliaro, F., Bearpark, M., Heyd, J. J., Brothers, E., Kudin, K. N., Staroverov, V. N., Keith, T., Kobayashi, R., Normand, J., Raghavachari, K., Rendell, A., Burant, J. C., Iyengar, S. S., Tomasi, J., Cossi, M., Rega, N., Millam, J. M., Klene, M., Knox, J. E., Cross, J. B., Bakken, V., Adamo, C., Jaramillo, J., Gomperts, R., Stratmann, R. E., Yazyev, O., Austin, A. J., Cammi, R., Pomelli, C., Ochterski, J. W., Martin, R. L., Morokuma, K., Zakrzewski, V. G., Voth, G. A., Salvador, P., Dannenberg, J. J., Dapprich, S., Daniels, A. D., Farkas, O., Foresman, J. B., Ortiz, J. V., Cioslowski, J., and Fox, D. J. (2013) *Gaussian 09*, revision D.01, Gaussian, Inc., Wallingford, CT.
(46) Case, D. A., Darden, T. A., Cheatham, T. E., III, Simmerling, C. L., Wang, J., Duke, R. E., Luo, R., Crowley, M., Walker, R. C., Zhang, W., Merz, K. M., Wang, B., Hayik, S., Roitberg, A., Seabra, G., Kolossvary, I., Wong, K. F., Paesani, F., Vanicek, J., Wu, X., Brozell, S. R., Steinbrecher, T., Gohlke, H., Yang, L., Tan, C., Mongan, J., Hornak, V., Cui, G., Mathews, D. H., Seetin, M. G., Sagui, C., Babin, V., and Kollman, P. A. (2008) *AMBER Tools*, version 1.0, University of California, San Francisco.
(47) Case, D. A., Darden, T. A., Cheatham, T. E., III, Simmerling, C. L., Wang, J., Duke, R. E., Luo, R., Walker, R. C., Zhang, W., Merz, K. M., Roberts, B., Hayik, S., Roitberg, A., Seabra, G., Swails, J., Goetz, A. W., Kolossváry, I., Wong, K. F., Paesani, F., Vanicek, J., Wolf, R. M., Liu, J., Wu, X., Brozell, S. R., Steinbrecher, T., Gohlke, H., Cai, Q., Ye, X., Wang, J., Hsieh, M.-J., Cui, G., Roe, D. R., Mathews, D. H., Seetin, M. G., Salomon-Ferrer, R., Sagui, C., Babin, V., Luchko, T., Gusarov, S., Kovalenko, A., and Kollman, P. A. (2012) *AMBER 12*, University of California, San Francisco.
(48) Case, D. A., Darden, T. A., Cheatham, T. E., III, Simmerling, C. L., Wang, J., Duke, R. E., Luo, R., Crowley, M., Walker, R. C., Zhang, W., Merz, K. M., Wang, B., Hayik, S., Roitberg, A., Seabra, G., Kolossváry, I., Wong, K. F., Paesani, F., Vanicek, J., Wu, X., Brozell, S. R., Steinbrecher, T., Gohlke, H., Yang, L., Tan, C., Mongan, J., Hornak, V., Cui, G., Mathews, D. H., Seetin, M. G., Sagui, C., Babin, V., and Kollman, P. A. (2010) *AMBER 11*, University of California, San Francisco.
(49) Dennington, R., Keith, T., and Millam, J. (2009) *GaussView*, version 5, Semichem Inc., Shawnee Mission, KS.
(50) Jorgensen, W. L., Chandrasekhar, J., Madura, J. D., Impey, R. W., and Klein, M. L. (1983) Comparison of Simple Potential Functions for Simulating Liquid Water. *J. Chem. Phys. 79*, 926−935.
(51) Smith, D. E., and Dang, L. X. (1994) Computer simulations of NaCl association in polarizable water. *J. Chem. Phys. 100*, 3757−3766.
(52) Beglov, D., and Roux, B. (1994) Finite Representation of an Infinite Bulk System: Solvent Boundry Potential for Computer Simulations. *J. Chem. Phys. 100*, 9050−9063.
(53) Joung, I. S., and Cheatham, T. E. (2008) Determination of alkali and halide monovalent ion parameters for use in explicitly solvated biomolecular simulations. *J. Phys. Chem. B 112*, 9020−9041.
(54) Noy, A., Soteras, I., Luque, F. J., and Orozco, M. (2009) The impact of monovalent ion force field model in nucleic acids simulations. *Phys. Chem. Chem. Phys. 11*, 10596−10607.
(55) Dupradeau, F.-Y., Pigache, A., Zaffran, T., Savineau, C., Lelong, R., Grivel, N., Lelong, D., Rosanski, W., and Cieplak, P. (2010) The R.E.D. tools: Advances in RESP and ESP charge derivation and force field library building. *Phys. Chem. Chem. Phys. 12*, 7821−7839.
(56) Wang, J., Wang, W., Kollman, P. A., and Case, D. A. (2006) Automatic atom type and bond type perception in molecular mechanical calculations. *J. Mol. Graphics Modell. 25*, 247−260.
(57) Pérez, A., Marchán, I., Svozil, D., Sponer, J., Cheatham, T. E., III, Laughton, C. A., and Orozco, M. (2007) Refinement of the AMBER Force Field for Nucleic Acids: Improving the Description of *α*/*γ* Conformers. *Biophys. J. 92*, 3817−3829.
(58) Cheatham, T. E., Cieplak, P., and Kollman, P. A. (1999) A modified version of the Cornell et al. force field with improved sugar pucker phases and helical repeat. *J. Biomol. Struct. Dyn. 16*, 845−862.
(59) Wang, J., Wolf, R. M., Caldwell, J. W., Kollman, P. A., and Case, D. A. (2004) Development and testing of a general amber force field. *J. Comput. Chem. 25*, 1157−1174.
(60) Zgarbová, M., Otyepka, M., Šponer, J. I., Mládek, A. T., Banáš, P., Cheatham, T. E., and Jurečka, P. (2011) Refinement of the Cornell et al. Nucleic Acids Force Field Based on Reference Quantum Chemical Calculations of Glycosidic Torsion Profiles. *J. Chem. Theory Comput. 7*, 2886−2902.
(61) Šponer, J., Cang, X., and Cheatham, T. E., III (2012) Molecular dynamics simulations of G-DNA and perspectives on the simulation of nucleic acid structures. *Methods 57*, 25−39.
(62) Case, D. A., Cheatham, T. E., Darden, T., Gohlke, H., Luo, R., Merz, K. M., Onufriev, A., Simmerling, C., Wang, B., and Woods, R. J. (2005) The Amber biomolecular simulation programs. *J. Comput. Chem. 26*, 1668−1688.
(63) Dans, P. D., Perez, A., Faustino, I., Lavery, R., and Orozco, M. (2012) Exploring polymorphisms in B-DNA helical conformations. *Nucleic Acids Res. 40*, 10668−10678.
(64) Miller, B. R., McGee, T. D., Swails, J. M., Homeyer, N., Gohlke, H., and Roitberg, A. E. (2012) MMPBSA.py: An Efficient Program for End-State Free Energy Calculations. *J. Chem. Theory Comput. 8*, 3314−3321.

DOI: 10.1021/bi501484m
Biochemistry 2015, 54, 2414−2428

(65) Brice, A. R., and Dominy, B. N. (2011) Analyzing the robustness of the MM/PBSA free energy calculation method: Application to DNA conformational transitions. *J. Comput. Chem. 32*, 1431−1440.
(66) Sharma, P., Manderville, R. A., and Wetmore, S. D. (2013) Modeling the Conformational Preference of the Carbon-Bonded Covalent Adduct Formed upon Exposure of 2′-Deoxyguanosine to Ochratoxin A. *Chem. Res. Toxicol. 26*, 803−816.
(67) Stavros, K. M., Hawkins, E. K., Rizzo, C. J., and Stone, M. P. (2014) Base-displaced intercalation of the 2-amino-3-methylimidazo 4,5-f quinolone N-2-dG adduct in the NarI DNA recognition sequence. *Nucleic Acids Res. 42*, 3450−3463.
(68) Mao, B., Gorin, A., Gu, Z., Hingerty, B. E., Broyde, S., and Patel, D. J. (1997) Solution Structure of the Aminofluorene-Intercalated Conformer of the syn [AF]-C8-dG Adduct Opposite a −2 Deletion Site in the NarI Hot Spot Sequence Context. *Biochemistry 36*, 14479−14490.
(69) Vaidyanathan, V. G., Liang, F., Beard, W. A., Shock, D. D., Wilson, S. H., and Cho, B. P. (2013) Insights into the Conformation of Aminofluorene-Deoxyguanine Adduct in a DNA Polymerase Active Site. *J. Biol. Chem. 288*, 23573−23585.
(70) Feng, B., Gorin, A., Hingerty, B. E., Geacintov, N. E., Broyde, S., and Patel, D. J. (1997) Structural Alignment of the (+)-trans-anti-Benzo[a]pyrene-dG Adduct Positioned Opposite dC at a DNA Template−Primer Junction. *Biochemistry 36*, 13769−13779.
(71) Rechkoblit, O., Kolbanovskiy, A., Malinina, L., Geacintov, N. E., Broyde, S., and Patel, D. J. (2010) Mechanism of error-free and semitargeted mutagenic bypass of an aromatic amine lesion by Y-family polymerase Dpo4. *Nat. Struct. Mol. Biol. 17*, 379−388.
(72) Lior-Hoffmann, L., Ding, S., Geacintov, N. E., Zhang, Y., and Broyde, S. (2014) Structural and Dynamic Characterization of Polymerase κ's Minor Groove Lesion Processing Reveals How Adduct Topology Impacts Fidelity. *Biochemistry 53*, 5683−5691.
(73) Broyde, S., Wang, L., Zhang, L., Rechkoblit, O., Geacintov, N. E., and Patel, D. J. (2007) DNA Adduct Structure−Function Relationships: Comparing Solution with Polymerase Structures. *Chem. Res. Toxicol. 21*, 45−52.
(74) Perlow-Poehnelt, R. A., Likhterov, I., Wang, L., Scicchitano, D. A., Geacintov, N. E., and Broyde, S. (2007) Increased flexibility enhances misincorporation temperature effects on nucleotide incorporation opposite a bulky carcinogen-DNA by a Y-family DNA polymerase. *J. Biol. Chem. 282*, 1397−1408.
(75) Shapiro, R., Ellis, S., Hingerty, B. E., and Broyde, S. (1998) Effect of Ring Size on Conformations of Aromatic Amine−DNA Adducts: The Aniline−C8 Guanine Adduct Resides in the B-DNA Major Groove. *Chem. Res. Toxicol. 11*, 335−341.
(76) Millen, A. L., Sharma, P., and Wetmore, S. D. (2012) C8-linked bulky guanosine DNA adducts: Experimental and computational insights into adduct conformational preferences and resulting mutagenicity. *Future Med. Chem. 4*, 1981−2007.
(77) Mu, H., Kropachev, K., Wang, L., Zhang, L., Kolbanovskiy, A., Kolbanovskiy, M., Geacintov, N. E., and Broyde, S. (2012) Nucleotide excision repair of 2-acetylaminofluorene- and 2-aminofluorene-(C8)-guanine adducts: Molecular dynamics simulations elucidate how lesion structure and base sequence context impact repair efficiencies. *Nucleic Acids Res. 40*, 9675−9690.
(78) Kowal, E. A., Seneviratne, U., Wickramaratne, S., Doherty, K. E., Cao, X., Tretyakova, N., and Stone, M. P. (2014) Structures of Exocyclic R,R- and S,S-N6,N6-(2,3-Dihydroxybutan-1,4-diyl)-2′-Deoxyadenosine Adducts Induced by 1,2,3,4-Diepoxybutane. *Chem. Res. Toxicol. 27*, 805−817.
(79) Wang, L., Hingerty, B. E., Shapiro, R., and Broyde, S. (2004) Structural and Stereoisomer Effects of Model Estrogen Quinone-Derived DNA Adducts: N6-(2-Hydroxyestron-6(α,β)-yl)-2′-deoxyadenosine and N2-(2-Hydroxyestron-6(α,β)-yl)-2′-deoxyguanosine. *Chem. Res. Toxicol. 17*, 311−324.
(80) Ruan, Q., Kolbanovskiy, A., Zhuang, P., Chen, J., Krzeminski, J., Amin, S., and Geacintov, N. E. (2002) Synthesis and Characterization of Site-Specific and Stereoisomeric Fjord Dibenzo[a,l]pyrene Diol Epoxide−N6-Adenine Adducts: Unusual Thermal Stabilization of Modified DNA Duplexes. *Chem. Res. Toxicol. 15*, 249−261.
(81) Baird, W. M., Hooven, L. A., and Mahadevan, B. (2005) Carcinogenic polycyclic aromatic hydrocarbon-DNA adducts and mechanism of action. *Environ. Mol. Mutagen. 45*, 106−114.
(82) Yan, S., Shapiro, R., Geacintov, N. E., and Broyde, S. (2001) Stereochemical, Structural, and Thermodynamic Origins of Stability Differences between Stereoisomeric Benzo[a]pyrene Diol Epoxide Deoxyadenosine Adducts in a DNA Mutational Hot Spot Sequence. *J. Am. Chem. Soc. 123*, 7054−7066.
(83) Rubbi, C. P., and Milner, J. (2001) Analysis of nucleotide excision repair by detection of single-stranded DNA transients. *Carcinogenesis 22*, 1789−1796.
(84) Cai, Y., Zheng, H., Ding, S., Kropachev, K., Schwaid, A. G., Tang, Y., Mu, H., Wang, S., Geacintov, N. E., Zhang, Y., and Broyde, S. (2013) Free Energy Profiles of Base Flipping in Intercalative Polycyclic Aromatic Hydrocarbon-Damaged DNA Duplexes: Energetic and Structural Relationships to Nucleotide Excision Repair Susceptibility. *Chem. Res. Toxicol. 26*, 1115−1125.
(85) Min, J.-H., and Pavletich, N. P. (2007) Recognition of DNA damage by the Rad4 nucleotide excision repair protein. *Nature 449*, 570−575.
(86) Geacintov, N. E., Broyde, S., Buterin, T., Naegeli, H., Wu, M., Yan, S., and Patel, D. J. (2002) Thermodynamic and structural factors in the removal of bulky DNA adducts by the nucleotide excision repair machinery. *Biopolymers 65*, 202−210.
(87) Gunz, D., Hess, M. T., and Naegeli, H. (1996) Recognition of DNA Adducts by Human Nucleotide Excision Repair: Evidemce for a thermodynamic probing mechanism. *J. Biol. Chem. 271*, 25089−25098.
(88) Sugasawa, K., Okamoto, T., Shimizu, Y., Masutani, C., Iwai, S., and Hanaoka, F. (2001) A multistep damage recognition mechanism for global genomic nucleotide excision repair. *Genes Dev. 15*, 507−521.
(89) Schärer, O. D. (2007) Achieving Broad Substrate Specificity in Damage Recognition by Binding Accessible Nondamaged DNA. *Mol. Cell 28*, 184−186.
(90) Kropachev, K., Ding, S., Terzidis, M. A., Masi, A., Liu, Z., Cai, Y., Kolbanovskiy, M., Chatgilialoglu, C., Broyde, S., Geacintov, N. E., and Shafirovich, V. (2014) Structural basis for the recognition of diastereomeric 5′,8-cyclo-2′-deoxypurine lesions by the human nucleotide excision repair system. *Nucleic Acids Res. 42*, 5020−5032.
(91) Maillard, O., Camenisch, U., Clement, F. C., Blagoev, K. B., and Naegeli, H. (2007) DNA repair triggered by sensors of helical dynamics. *Trends Biochem. Sci. 32*, 494−499.
(92) Yang, W. (2006) Poor base stacking at DNA lesions may initiate recognition by many repair proteins. *DNA Repair 5*, 654−666.
(93) Reeves, D. A., Mu, H., Kropachev, K., Cai, Y., Ding, S., Kolbanovskiy, A., Kolbanovskiy, M., Chen, Y., Krzeminski, J., and Amin, S. (2011) Resistance of bulky DNA lesions to nucleotide excision repair can result from extensive aromatic lesion−base stacking interactions. *Nucleic Acids Res.*, gkr537.
(94) Mu, H., Kropachev, K., Chen, Y., Zhang, H., Cai, Y., Geacintov, N. E., and Broyde, S. (2013) Role of Structural and Energetic Factors in Regulating Repair of a Bulky DNA Lesion with Different Opposite Partner Bases. *Biochemistry 52*, 5517−5521.
(95) Hanawalt, P. C., and Spivak, G. (2008) Transcription-coupled DNA repair: Two decades of progress and surprises. *Nat. Rev. Mol. Cell Biol. 9*, 958−970.

DOI: 10.1021/bi501484m
Biochemistry 2015, 54, 2414−2428